

DESIGN, FABRICATION, AND APPLICATIONS OF MULTI-MODE NANOELECTROMECHANICAL SYSTEMS

A THESIS SUBMITTED TO
THE GRADUATE SCHOOL OF ENGINEERING AND SCIENCE
OF BILKENT UNIVERSITY
IN PARTIAL FULFILLMENT OF THE REQUIREMENTS FOR
THE DEGREE OF
MASTER OF SCIENCE
IN
MECHANICAL ENGINEERING

By
Atakan Bekir Arı
July 2017

DESIGN, FABRICATION, AND APPLICATIONS OF MULTI-
MODE NANOELECTROMECHANICAL SYSTEMS

By Atakan Bekir Arı

July 2017

We certify that we have read this thesis and that in our opinion it is fully adequate,
in scope and in quality, as a thesis for the degree of Master of Science.

Mehmet Selim Hanay(Advisor)

Haluk Klah

Onur zcan

Approved for the Graduate School of Engineering and Science:

Ezhan Karasan
Director of the Graduate School

ABSTRACT

DESIGN, FABRICATION, AND APPLICATIONS OF MULTI-MODE NANO-ELECTROMECHANICAL SYSTEMS

Atakan Bekir Ari

M.S. in Mechanical Engineering

Advisor: Mehmet Selim Hanay

July 2017

Miniaturization of systems allowed wide spread consumer use of microelectronics, integrated circuits and MEMS based sensors. Thanks to the advancement in microfabrication methods, it is possible to build structures with submicron dimensions. The integration of electronic control to these submicron structures started the NEMS field. Due to their minuscule dimensions and very high frequency response, NEMS can sense external perturbations with unprecedented sensitivity. This made NEMS excellent candidates for sensor applications. NEMS are starting to evolve from academic research tools to become mass produced and large scale integrated sensing devices.

Information extracted from the higher order modes further increase the capabilities of NEMS. In order to attain this extra information, we fabricated NEMS that can reach higher order mechanical modes. Every step of fabrication was done at Bilkent University research facilities such as UNAM and ARL. To pattern the submicron feature sizes, we relied on electron beam lithography. Thermal and electron beam evaporators were deployed for metallization of contacts and etch mask. In order to suspend the doubly clamped beams, we developed anisotropic silicon nitride and isotropic silicon dry etch recipes. At each step of the fabrication, tools such as SEM and stylus profilometer was utilized for characterization. Fabricated NEMS were wirebonded to printed circuit boards for detection.

Electrothermal actuation, an integrated method, was chosen to drive the nanomechanical resonator to its higher order modes. Piezoresistive down-mixing, another integrated method to complement the actuation, was used to detect the resulting nanomechanical motion. We used high frequency electronic equipment

to detect RF range responses of our NEMS. Using these NEMS, we studied two novel applications on intermodal and mechanical coupling.

First, we investigated intermodal coupling effect of doubly clamped beams in order utilize this coupling effect in higher order mode detection. When a doubly clamped beam is excited at its resonance frequency, every other mode of the device gets tuned. This occurs due to the clamping on both sides preventing longitudinal elongation and causing a stress on the beam. Using intermodal coupling method, we probed higher order modes of a nanomechanical resonator while tracking the fundamental frequency at the same time. We were able to detect mechanical modes up to 840 MHz, well out of the detection limit of our setup. We propose intermodal coupling as a novel detection method to acquire frequency response of NEMS at higher order modes which can not be detected with conventional methods.

Finally, we studied nano scale energy sinks that absorb energy from a another structure. Energy sinks are linear oscillators that can trap the energy of a nearby structure within their phase space. When the natural frequency of these sinks are distributed optimally, finite number of sinks can mimic absorption of infinite sinks. We envisioned a real time dissipation controlled NEMS platform by deploying energy sinks. In order to test energy sink performance at nano scale, we devised an experimental setup, comparing identical nanomechanical resonators with and without energy sinks. We have shown that energy sinks successfully absorb energy of a resonator at nanoscale.

Keywords: NEMS, Nanofabrication, Electron Beam Lithography, Reactive Ion Etching, Electrothermal Actuation, Piezoresistive Down-Mixing, Nanomechanics, Mode-Coupling, Energy Sinks, Quality Factor Modulation.

ÖZET

ÇOK MODLU NANOELEKTROMEKANİK SİSTEMLERİN TASARIM, ÜRETİM, VE UYGULAMALARI

Atakan Bekir Arı

Makine Mühendisliği, Yüksek Lisans

Tez Danışmanı: Mehmet Selim Hanay

Temmuz 2017

Sistemlerin minyatürleştirilmesi ile birlikte mikroelektronik, entegre devre, ve MEMS bazlı sensorler geniş marketlere açılabilir. Mikrofabrikasyon tekniklerindeki gelişmeler sayesinde artık bir mikrondan daha küçük boyutlu yapılar üretilebiliyor. Bu yapıların elektronik cihazlarla kontrolü NEMS alanının başlamasına sebep olmuştur. NEMS, çok küçük boyutları ve yüksek frekanslı tepkileri sayelerinde harici uyarıları rakipsiz bir hassaslıkla ölçülebilir. Bu özellikler sayesinde NEMS, sensor uygulamaları için mükemmel bir seçenektir. Günümüzde NEMS, akademik araştırma araçları olmaktan çıkıp seri imalat ile üretilip geniş ölçekte tümleşen cihazlar haline geliyor.

Yüksek modlardan elde edilen bilgi NEMS'lerin kabiliyetlerini oldukça artırıyor. Bu sebeple, yüksek mod uygulamalarında kullanılmak üzere bu modlara ulaşılabilen NEMS ürettik. Bu cihazların üretimi, UNAM ve ARL gibi Bilkent Üniversitesi araştırma laboratuvarlarında gerçekleştirildi. Mikrondan küçük yapıların üretimi için elektron demeti litografisinden yararlandık. Termal ve elektron demeti eriticileri ise metalizasyon aşamalarında kullanıldı. Çift ankastrelili yapıların serbest bırakılması ise anisotropik silikon nitrat ve isotropik silikon kuru aşındırma teknikleriyle gerçekleştirildi. Üretimin her adımında SEM ve profilometre ile nitelendirme yapıldı. Üretimi tamamlanan cihazlar ölçümler için baskılı devre kartlarına tutturuldu.

Tümleşik bir teknik olan elektrotermal sürme NEMS'leri yüksek modlara sürmek için kullanıldı. Oluşan nanomekanik hareketlerin ölçümü ise piezorezistif frekans-aşağı-kaydırma ile yapıldı. Ölçümleri yüksek frekanslı elektronik ekipman ile yaptık. Bu NEMS'leri kullanarak iki yeni uygulama üzerinde çalışma yaptık.

İlk olarak, modlar arası eşleşme etkisini yüksek modlarda kullanmak üzere çift ankastreli girişler üzerinde çalıştık. Çift ankastreli bir giriş rezonans frekansında sürüldüğü zaman diğer bütün modları değişime uğrar. Bu etkinin sebebi çift ankastreli yapının girişin uzamasını engelleyerek giriş üzerine bir gerilim uygulamasıdır. Bu modlar arası eşleşme metodunu kullanarak, bir nanomekanik rezonatörü doğal frekansında sürerken, yüksek modlarını sırasıyla yokladık. Ölçüm ekipmanımızın limitinin çok üstünde olan 840 MHz'e kadar mekanik mod ölçümü yapmayı başardık. Modlar arası eşleşme metodunu ölçümü zor olan yüksek modların ölçümü için yeni bir araç olarak sunuyoruz.

Son olarak, yapıların enerjisini emen enerji sönümleyicileri nano boyuta adapte ettik. Enerji sönümleyiciler yakınlarındaki yapıların enerjilerini kendi faz uzaylarında hapsedebilen lineer osilatörlerdir. Bu enerji sönümleyicilerin frekansları optimum bir şekilde düzenlendiğinde sonsuz sayıdaki sönümleyicinin etkisini sonlu sayıda sönümleyici ile taklit edebiliriz. Bu cihazları kullanarak gerçek zamanlı enerji kaybı kontrolü yapalabilen bir NEMS platformu tasavvur ettik. Bu yapıları test etmek amacıyla deneysel bir düzenek kurduk. Enerji sönümleyicili ve enerji sönümleyicisiz NEMS'leri karşılaştırarak enerji sönümleyicilerin nano boyutta enerji kaybı kontrolü için kullanılabileceğini gösterdik.

Anahtar sözcükler: NEMS, Nanofabrikasyon, Elektron Işını Litografisi, Reaktif İyon Aşındırma, Elektrottermal Sürüm, Piezorezistif frekans-aşağı-kaydırma, Nanomekanik, Mod Eşleşme, Enerji Sönümleyici, Q Faktörü Modülasyonu.

Acknowledgement

First of all, I would like to thank my MS thesis advisor M. Selim Hanay for his guidance and generous support during my graduate study. It wouldn't be an exaggeration if I said meeting Dr. Hanay changed my life completely. His work altered my view of mechanical engineering and he inspired me to become a better engineer and a scientist. It is a great honor for me to be one of his first graduate students.

I would like to thank my MS thesis committee, Prof. Onur Özcan and Prof. Haluk Külah for their time and valuable suggestions. I'm grateful to Dr. Cenk Yanık for all his help and invaluable tips on fabrication and e-beam lithography. I want to thank Prof. Kamil Ekinci for all the discussions and for our work together. I learned a lot from him during our time in Bilkent and Boston University. Ahmet can Kırhoğlu, Vural Kara, Josh Javor, and Pınar Karayaylalı; thank you for making my brief time in Boston memorable. Pınar, thank you for being there for me during the hardest times and lend an ear whenever I needed to vent.

I want to thank my brilliant colleagues Mustafa Çağatay Karakan, Selçuk Oğuz Erbil, Ezgi Orhan, Hande Aydoğmuş, Mehmet Kelleci, Levent Aslanbaş, and Mert Yüksel from Hanay Research Group. It was my privilege to share the lab and a part of my life with you. Thank you all for your support and friendship. Çağatay, you have been one of my best friends for a very long time now. I'm glad we got to work together in graduate school and I'm glad we will continue to do so. Selçuk, you are one of the few people whom I would trust with my NEMS; thank you for your selfless support and help during fabrication.

I have shared the hardships of graduate school with a lot of amazing people here in Bilkent University Mechanical Engineering Department. Anıl Alan, Buğra Türeyen, Arda Balkancı, Serdar Taze, Hossein Alijani, Negin Musavi, Alper Özoğul, Müge Özcan, and even though not technically a grad student Furkan Ayhan; thank you all for your friendship and for all the thoughtful discussions

we had. I want to thank our administrative assistant Ela Özsoy for bearing with my most ridiculous requests all these years from undergrad to graduate school.

As an important part of this MS study was spent in the cleanroom, I want to thank staff and personnel of UNAM and ARL. Especially Murat Güre, Mustafa Güler, Hakan Sürel, Semih Bozkurt, Abdullah Kafadenk. Thank you for keeping everything running and ready. Without your expertise on microfabrication I wouldn't be able to fabricate NEMS at Bilkent University. I'd like to also acknowledge Ufuk Turan's help with the fabrication of the printed circuit boards.

Finally, I would like to express my gratitude to my family. My dear brothers Hakan and Sinan, thank you for being there for me whenever I needed and giving me strength to go on no matter what. Mom and Dad, thank you for believing me and pushing me to become a better person. Your unconditional love and support made me what I am today. Everything I aspire to be, I owe it to you.

We acknowledge support from TÜBİTAK (grant number 113E600) for part of the work presented here.

Contents

- 1 Introduction** **1**
- 1.1 Nanoelectromechanical Systems 2
- 1.2 Flexural Vibrations of Doubly
 Clamped Beams 3
- 1.3 Thesis Outline 6

- 2 Fabrication Methods for NEMS** **8**
- 2.1 Design 9
- 2.1.1 Design Rationale 10
- 2.2 Sample Preparation 11
- 2.3 Lithography 14
- 2.3.1 Photolithography 14
- 2.3.2 Electron Beam Photolithography 18
- 2.4 Evaporation 24

2.4.1	Thermal Evaporation	26
2.4.2	Electron Beam Evaporation	29
2.5	Lift-off	29
2.6	Etching	32
2.6.1	Wet Etching	32
2.6.2	Dry Etching	33
2.7	Wirebonding	38
2.8	Characterization	39
2.8.1	Microscopy	40
2.8.2	Profilometer	41
2.8.3	Probe Station	42
2.9	Fabrication Steps of Silicon Nitride Devices	43
3	Transducers for NEMS	45
3.1	Electrothermal Actuation	46
3.2	Piezoresistive Detection	47
3.3	Detection Setup	49
4	Applications	52
4.1	Intermodal Coupling Detection for Higher Order Nanomechanical Modes	52

<i>CONTENTS</i>	xi
4.2 Nanomechanical Resonator Platform with Tunable Quality Factor	62
5 Conclusion and Future Work	68
A RCA Clean	79
B E-beam Lithography Operation Checklist	81

List of Figures

1.1	Two examples of NEMS devices fabricated during this study with widths and thicknesses smaller than a micrometer.	3
1.2	A doubly clamped beam with length L , width w and thickness t	4
1.3	Mode shapes of a doubly clamped beam for $n=1,2,3,4$	5
2.1	A multi layered GDSII design	10
2.2	GDSII design of contact pads (a) patterned onto a 5 inch soda lime photomask (b) by a mask writer.	15
2.3	Exposure Process and effect of UV radiation on positive resist (a) and negative resist (b).	17
2.4	Dose factors for the same design. (a) has no proximity correction while (b) is proximity corrected.	20
2.5	Dose test characterization by SEM.	22
2.6	SEM image of a NEMS device that had gone through 2 alignment procedures.	24
2.7	Step coverage of evaporation and sputtering.	26

2.8	Few example of boats and crucibles used for evaporation.	27
2.9	Inside of a thermal evaporator chamber.	28
2.10	Inside of an e-beam evaporator chamber.	30
2.11	Lift-off mechanism.	31
2.12	Unsuccessful lift-off procedures.	32
2.13	Stiction of a silicon beam after HF based oxide wet etch.	33
2.14	Schematic of an ICP chamber.	35
2.15	Etch recipe development steps.	38
2.16	Photograph of a wirebonder during bonding operation (a). SEM micrograph of a wirebonded device (b).	39
2.17	A silicon chip with dozens of NEMS, wirebonded to a 5 port printed circuit board.	40
2.18	Images of a NEMS taken with optic microscopy (a), SEM (b) and tilted view with SEM (c).	41
2.19	Stylus profilometer measurements of sample undergone a 100 cycle DRIE etch showing μm deep trenches.	42
2.20	Fabrication steps of silicon nitride devices - part A	43
2.21	Fabrication steps of silicon nitride devices - part B	44
3.1	AC (a) and DC operation (b) schematics of electrothermal actuation.	47
3.2	DC biasing (a) and AC biasing(c) for signal down-mixing	48

3.3	Simplified Dbox architecture (a) and its connections to a typical NEMS device.	49
3.4	Mechanical response of a NEMS around 74.8 MHz detected using Dbox.	50
3.5	Comparison of the response of one of the first iteration of devices	50
4.1	Scanning electron micrograph of a nanomechanical resonator . . .	53
4.2	Resonant response for the 1st mode at 20 <i>mTorr</i>	54
4.3	Closed loop intermodal coupling measurements between 1 st mode and higher order modes	55
4.4	A similar NEMS fabricated at Sabanci University as a collaboration.	57
4.5	Open loop measurement from 1 to 50 MHz in air	58
4.6	Closed-loop intermodal coupling measurements using the first three out-of-plane modes.	58
4.7	PLL mode-coupling measurements between 1 st and 2 nd mode . . .	60
4.8	Macro scale (a) model versus nano scale (b) model of energy sink interaction.	63
4.9	Resonance frequency vs. energy sink length	64
4.10	Top and tilted view SEM images of a NEMS with frequency distributed energy sinks.	65
4.11	Detection scheme of the devices and first fundamental mode driven to nonlinearity.	65
4.12	Energy sinks experimental results.	66

List of Tables

1.1	Higher order solutions of a doubly clamped beam.	5
2.1	PMMA bilayer spin coating recipe for 300 <i>nm</i> thick film.	19
2.2	PMMA development procedure.	21
2.3	Etch recipes developed for silicon nitride and silicon for STS ICP.	37
4.1	Quality Factors of the first 5 modes and two ultra-high frequency	59
4.2	Features observed during the PLL on first and second mode, ranging from 40 to 150 MHz.	61

Chapter 1

Introduction

First electronic computers were as big as rooms, weighed dozens of tons, and required thousands of watts to operate them back in 1940s; whereas today, we can fit a “computer” that has more computational power than the Apollo 11 ground computers had when they put a man on the moon. These pocket computers also have numerous sensors in them: accelerometers, gyroscopes, proximity sensors, barometers, GPS trackers and many more wondrous small machines. The widespread availability of such technology can be attributed to the miniaturization of systems which have been going on with an astonishing pace starting with the rise of the integrated circuit (IC) industry during the 1960s. We are trying to fit more and more into smaller and smaller spaces ever since.

This miniaturization effort of course brings challenges with it. Foreseen or completely unexpected obstacles arise at smaller scales. Even though the laws of physics do not change fundamentally; dominant forces do. Surface tension and capillary forces start to become prevalent over gravitational forces. Effectiveness of actuators and batteries diminishes as surface to volume ratio increases and so on. On the other hand, the incentives to scale down are enticing. There are economic reasons of course: smaller things require less materials to build, less energy to power which decreases the costs altogether. From a scientific standpoint however, small scale allows us to breakdown macro laws in physics and chemistry

allowing development of new paradigms.

Following the developments in IC industry and microfabrication methods, electronically controlled micro scaled mechanical machines were built and were classified as microelectromechanical systems [1]. MEMS field was a great success and quickly dominated the consumer electronics market with inkjet printers, accelerometers, electronic filters and many other sensor applications. Yet, as Feynman said there is still “plenty of room at the bottom” [2]. Thus, we moved on to the next big thing, or rather the *small* thing, ahead: nanoelectromechanical systems.

This thesis is a result of a work that hoped to protrude a tiny dent in the vast research field of NEMS. First and foremost goal was to fabricate functional NEMS at Bilkent University; specifically, NEMS that can reach higher order modes deep in to the microwave range. In order to achieve this goal we relied on the cleanroom and microfabrication capabilities of National Nanotechnology Research Center (UNAM) which is located in Bilkent University Campus. Second part of this study was to use these “homemade” NEMS for multi-mode sensing applications where information extracted from such modes would be utilized.

1.1 Nanoelectromechanical Systems

NEMS are electronically controlled mechanical machines with at least one dimension smaller than a micrometer. They can be considered as even smaller MEMS. Starting with first demonstrations in 1996 [3], NEMS field grew rapidly and has been very active. Due to their nanoscale dimensions, NEMS offer interesting capabilities such as: resonance frequencies in microwave range [4], Quality (Q) factors in the tens of thousands [5], heat capacities below yoctocalories [6], effective masses in the femtograms [7] and so on. Many breakthroughs in fundamental physics studies [8], [9] have been achieved with NEMS. Alongside these studies, there is a wide range of demanding sensor applications that utilize NEMS such as gas sensing [10, 11, 12], single-molecule mass sensing [13], single-protein [14]

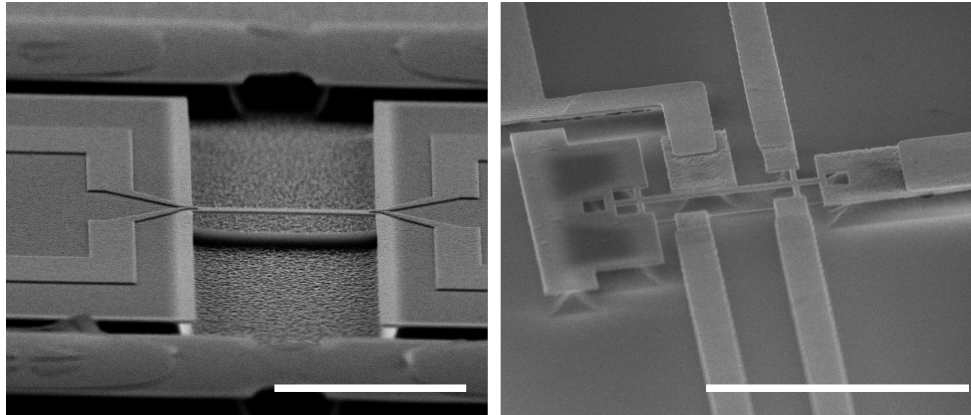


Figure 1.1: Two examples of NEMS devices fabricated during this study with widths and thicknesses smaller than a micrometer. Scale bars are $10\ \mu\text{m}$.

and neutral-particle [15] mass spectrometry, force sensing [16, 17], and inertial imaging [18].

In recent years, NEMS technology has begun to evolve from academic laboratories to be developed in microelectronic manufacturing and testing centers. It is now possible to produce thousands of NEMS devices within the same fabrication process and use them in scientific applications [19].

1.2 Flexural Vibrations of Doubly Clamped Beams

There are many different nanomechanical structures that are being used in sensor applications such as doubly clamped beams, cantilevers, free-free beams, 2D membranes, and so on. In this study we used doubly clamped nanomechanical resonators as the mechanical part for our NEMS.

Fig 1.2 shows a doubly clamped beam with length L , width w , and thickness t . Small displacements of long thin beams ($t/L \ll 1$) can be modeled with Euler-Bernoulli beam theory [20]. Assuming the beam is vibrating in an out-of-plane motion in the direction of y axis with a displacement of $U(x,t)$:

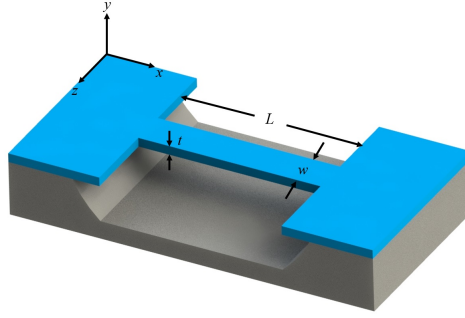


Figure 1.2: A doubly clamped beam with length L , width w and thickness t .

$$\rho wt \frac{\partial^2 U}{\partial t^2} = -\frac{\partial^2}{\partial x^2} EI \frac{\partial^2 U}{\partial x^2}, \quad (1.1)$$

where ρ is the density, E is Young's Modulus, and $I = wt^3/12$ is the bending moment of inertia. Due to the clamping on both ends the boundary conditions of the beam are $U(0) = U(L) = 0$ and $U'(0) = U'(L) = 0$. Solutions of the equation 1.1 are then in the form:

$$U_n(x, t) = (A_{1n}(\cos \beta_n x - \cosh \beta_n x) + A_{2n}(\sin \beta_n x - \sinh \beta_n x))e^{-i\omega_n t}, \quad (1.2)$$

where eigenvectors β_n satisfies $\cos \beta_n L \cosh \beta_n L = 1$. Solutions for higher modes are given on table 1.1. The angular frequency ω_n and fundamental frequency of the first mode f_1 is given by [21]:

$$\omega_n = \sqrt{\frac{EI}{\rho wt}} \beta_n^2, \quad (1.3)$$

$$f_1 = \frac{\omega_1}{2\pi} = 1.05 \sqrt{\frac{E}{\rho}} \frac{t}{L^2}. \quad (1.4)$$

The eigenfunctions U_n can be normalized to the beam length such that:

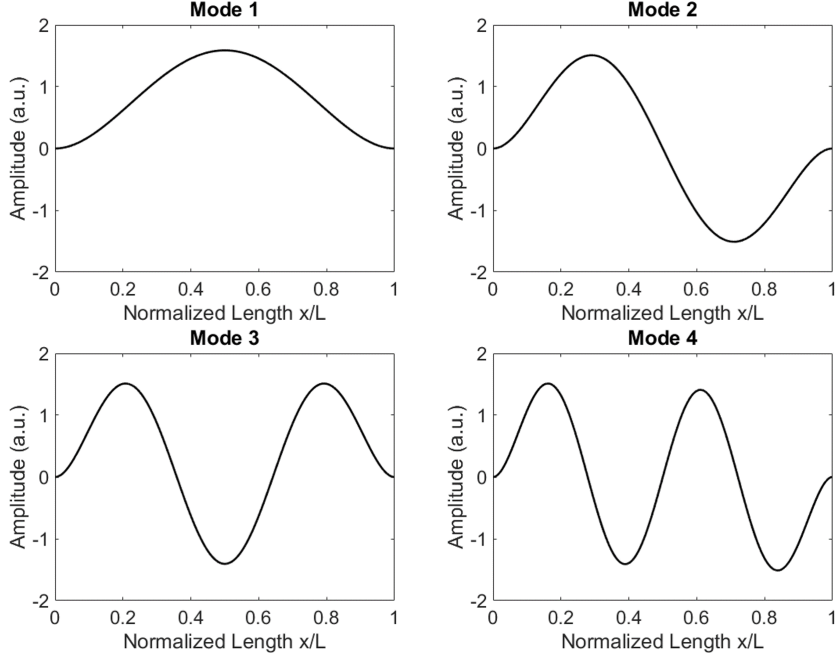


Figure 1.3: Mode shapes of a doubly clamped beam for $n=1,2,3,4$.

$$\int_0^L U_n(x)U_m(x)dx = L^3\delta_{mn}. \quad (1.5)$$

Finally an arbitrary solution can be written as:

$$U(x,t) = \sum_{n=1}^{\infty} a_n(t)U_n(x). \quad (1.6)$$

where a_n are dimensionless amplitudes. First four mode shapes of doubly clamped beam is given on figure 1.3.

Table 1.1: Higher order solutions of a doubly clamped beam. Recreated using data from [21].

	n=1	2	3	4
$\beta_n L$	4.730	7.8532	10.9956	14.1372
ω_n/ω_1	1	2.756	5.404	8.933
A_{1n}/L	-1	-1	-0,9988	-1
A_{2n}/L	0.9825	1.0008	0.9988	1.0000

1.3 Thesis Outline

Chapter 1 will serve as an introduction to nanoelectromechanical systems including a brief summary of the recent developments in the field, applications, and advantages of NEMS. A theoretical background on flexural vibrations of doubly clamped beams at nanoscale will be presented.

In Chapter 2, I will explain the microfabrication methods we used to build NEMS. Starting with a brief historical background on integrated circuit(IC) industry, each fabrication step that was used during this MS study will be explained including the working principles of the procedures. Steps are roughly in the order of a fabrication process of a NEMS; starting from substrate cleaning procedures to final step of wirebonding of a finished device to a printed circuit board. Furthermore, process development steps for procedures such as dry etch recipe preparation, electron beam lithography dose testing will be discussed on a practical level. Finally, detailed step by step fabrication process of a NEMS is given with each step visualized layer by layer in 3D. This chapter might serve as a guide for a graduate student who is just delving into the world micro/nanofabrication as well.

In Chapter 3, transducer mechanisms used for our NEMS will be explained. Electrothermal actuation is a tool to drive NEMS to higher order modes by Joule heating a bilayer structure. Advantages and drawback of this method will be discussed. In order to detect the nanomechanical motion of these sensors, piezoresistive down-mixing method was utilized. The geometric and material piezoresistivity will be explained. Drawbacks of DC biasing and the need for frequency down-mixing will be addressed. Finally, the electronic instrumentation used for the measurements will be discussed.

Chapter 4 presents two novel NEMS applications done during my MS studies. Intermodal Coupling, a new method to detect higher order modes of a nanomechanical resonator, will be discussed. The second application is on Q factor control of nanomechanical systems based on a mesoscopic work done on linear

energy absorbing oscillators called *energy sinks*. Theories, experimental setups and results of these work will be explained.

The final chapter will serve a summary and outlook to this M.S. thesis. Possible improvements and future works will be discussed for the applications mentioned in this work and a very brief information on other applications that are still undergoing at the time this thesis was completed.

Chapter 2

Fabrication Methods for NEMS

Microfabrication is an engineering discipline that covers the methods for fabrication for integrated circuits, microelectronics, MEMS, NEMS, and other related nanotechnology fields [22]. Dimensions of interest for microfabrication varies from atomically thin layers to hundreds of micrometers. With the integration of photolithography into microfabrication in 1960s [23], the IC industry grew rapidly alongside with microfabrication. While closely related to IC industry, very-large-scale integration (VLSI) deals with the design problem of fitting billions of transistors on a semiconductor chip while microfabrication deals with how to fabricate those transistors. First transistor was invented in 1947 at Bell Labs and after only 70 years, 14 *nm* minimum feature sized chips with billions of transistors are in the market for consumer use.

Nanofabrication is often used as a term to define fabrication methods for devices with minimum feature sizes lower than 100 *nm* [24]. Nanofabrication can be divided in to two major branches: top-down and bottom-up fabrication. An analogy for top-down fabrication would be chiseling a marble block to remove unnecessary parts to obtain a statue while the bottom-up fabrication rely on self organization and precursors to add materials to create the devices. While both have different advantages and disadvantages this work mostly focuses on top-down fabrication methods.

All of the devices mentioned in this work was fabricated at Bilkent University affiliated facilities such as National Nanotechnology Research Center (UNAM) and Advanced Research Laboratories (ARL). This work will not include comparison between every available microfabrication method, instead it will focus solely on the procedures used. Besides, information such as the cost of individual steps used, as important as it is especially for the industry, is out of scope of this work as the first and foremost requirement to choose a method was the availability of that method at the facilities. Further information on microfabrication techniques can be found in the literature as there are many great sources available [25], [26], [27], [22].

2.1 Design

Similar to manufacturing, microfabrication requires detailed planning and designing. *Layers* are used to represent each physical stack of materials. It is important to understand and visualize these layers to comprehend the flow and logic of each step of microfabrication. By adding or subtracting materials from these layers a final functional device is created. In this work GDSII (Graphic Data system) file format, which is currently the defacto IC industry standard, was used. In order to organize and create these layers, GDSII editors can be used. There are many GDSII editors available in the market and a few that have been used in this work are Clewin, Layout Editor, and Elphy Plus GDSII editor.

During design process the operator should take into consideration the fabrication limitations and feasibility before proposing a design. For example, fabricating very large contact pads ($>200 \mu m$) with electron beam lithography would take a lot of time and when there are 100 devices on a chip, it becomes unpractical. Instead, contact pad layer can be realized with photolithography and the device layer can be aligned later using electron beam lithography. Another example would be minimum feature sizes and error tolerances. For example, electron beam lithography device at UNAM has an error of $50 nm$ for each alignment procedure due to manual alignment procedure. In this case feature sizes smaller than 50

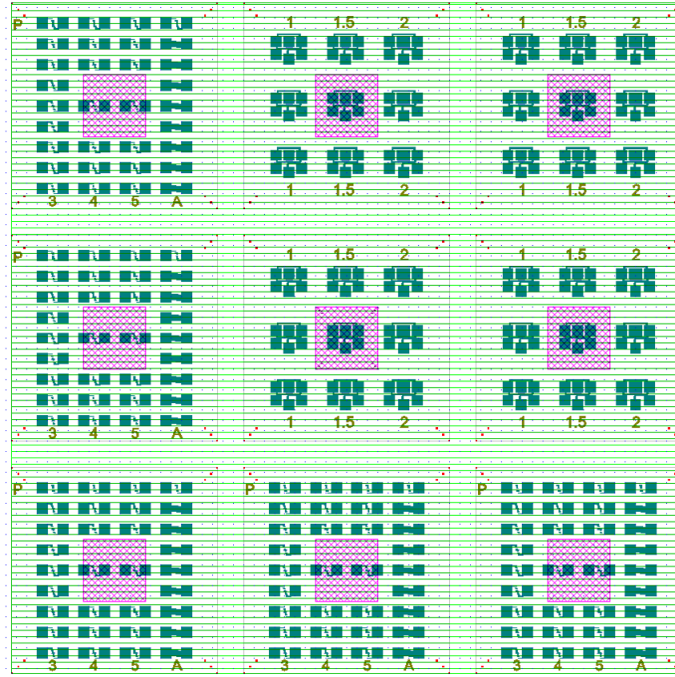


Figure 2.1: A multi layered GDSII design. Each layer is represented by different color and texture. Often numbers and markers are added for easier identification.

nm on different layers could not be fabricated reliably.

2.1.1 Design Rationale

The goal was to design mechanical resonator that can reach higher order modes. The doubly clamped beam was chosen instead of other mechanical structures because of the selected integrated transducers (electrothermal actuation and piezoresistive detection) which were to be placed in separate ends of the resonator to prevent any cross-talk between the transducers. Another incentive was that doubly clamped beams are established in the field and are used frequently for mass sensing applications [13, 14] and as a research group we have more experience with doubly clamped beams. In order to prevent any impedance mismatch with 50Ω detection equipment our integrated transducers were also needed to be 50Ω . In order to achieve this we designed the Au electrodes to have $50 \pm 10 \Omega$.

Device layer of our choice was low pressure chemical vapor deposition grown

silicon nitride which was commercially available and purchased from a supplier. First of all due to our transducers we needed an insulator device layer to prevent any shorts for the electronic circuit. A material with low thermal expansion coefficient was required compared to Au as the actuation mechanism depended on it [28]. Relatively low cost, good thermal resistance, and high Young's modulus made silicon nitride our choice of device layer instead of other common device layers such as SOI, SiC, SiO₂.

The high frequency responses of NEMS increase the detection speeds [10] and also has shown to increase the Q factor for bio-sensing applications [29]. Yet, with very high fundamental frequencies the higher order modes quickly get into microwave range and is not always easy to detect. In order to utilize these higher order modes and still attaining the high frequency response, we decided to keep our devices fundamental mode around 10 MHz. Since the device thickness was fixed from the supplier we determined the length of our initial devices at 10 μm which resulted in approximately 13 MHz fundamental frequency following the equation 1.3.

Our fabrication iterations showed that with 10 μm beams we can fit 4 modes under 100 MHz which will be useful for our mass sensing applications while at the same time allowing 13 MHz fundamental frequency for high speed measurements (figure 3.5).

2.2 Sample Preparation

Sample preparation is one of the most important steps of any fabrication process. There are many possible sources for contaminants which can lead for undesired results during fabrication such as airborne particles in the atmosphere, solvent stains, dust from the environment, skin flakes from the operators, etc. For example a strand of human hair, which is around 75-150 μm in diameter, left on a substrate before spin coating would render a photoresist layer useless. Moreover, there are many contaminants that are larger than the minimum feature size of

the devices that could seriously tamper with the fabrication. For example a 64-kB dynamic memory chip has a minimum feature size of $2.5 \mu\text{m}$ and could only tolerate $0.25 \mu\text{m}$ particles in the atmosphere [27].

To prevent all these sources from tainting the samples, fabrication must be done in specialized laboratories called *cleanrooms* which are enclosed areas where pressure, temperature, humidity and airborne particles are constantly controlled and regulated. Clean rooms are classified depending on the average particle size per cubic foot in the environment. The facilities of UNAM are 100 class clean rooms based on the U.S. federal standards. Furthermore, users should wear appropriate gear and follow gowning procedures to enter clean rooms. At all times, samples must be handled with utmost care, the device layers on top of the substrates should not be touched or scratched.

Even though clean rooms are absolutely necessary for microfabrication as a preventative measure for contamination they are not enough. Newly grown or commercially obtained wafers and samples that are being reused after certain procedures must go under a series of cleaning steps in order to get rid of any organic, ionic, or native oxide residues on the surface. For instance, when silicon wafers are not used for a certain amount of time; the surface atoms reacts with the oxygen in the atmosphere, creating a thin oxide layer. If an operator tries to deposit contact pads on top of such sample, assuming the sample is clean, those pads will not be electronically connected to silicon surface due to the insulating oxide layer in between.

The samples used in this work had gone through RCA wet clean procedure when first obtained. RCA clean was developed by Werner Kern while working at Radio Corporation of America in 1965 [30]. RCA clean has become the industry standard and used for new wafers out of the box and also before high temperature treatments such as oxidation, diffusion and so on. It is a two-step cleaning procedure where RCA-1 strips organic residues and RCA-2 ionic contaminants of the substrate. RCA-1 is particularly useful to clean samples after a failed photolithography step as it strips away all the organic photoresist residues. Steps and solvent ratios of the procedure could be modified and optional steps could be

added depending on the fabrication. Both RCA-1 and RCA-2 procedures leave a thin oxide layer on top of the surface; therefore, a third step of a quick HF dip is necessary to get rid of the oxide layer. If the samples are visibly contaminated, a piranha solution (a mixture of sulfuric acid and hydrogen peroxide) can be applied as preliminary cleaning. A step by step RCA clean procedure, based on [31], used in this work on newly acquired wafers are shown on appendix A.

If we consider RCA a *hard* clean for newly acquired wafers, there is also a *soft* cleaning procedure that involves sequential rinsing of the sample with acetone, isopropanol alcohol (IPA) and deionized (DI) water. This procedure should be applied after almost all steps of fabrication, excluding when there is an organic layer on the surface or there are suspended structures. Sample should be soaked in an acetone bath and then rinsed with flowing acetone. This step should be repeated using IPA. The sample must be rinsed with a DI water gun or flowing DI water afterwards. Finally, the sample must be dried with a nitrogen gun. If necessary a 1 minute 120 °C bake could be applied to get rid of humidity. The operator must be swift during these steps and should not allow any of the solvents to evaporate on the substrate as it could leave residues.

Commercially available wafers usually come in as 4 or 6 inch discs. While in IC industry even larger wafers are used during fabrication, for research and prototyping purposes smaller samples are desirable most of the time since they are easier to handle and during development many samples might get destroyed. In this work 10 mm x 10 mm square samples were used for both development stages and final devices; since the NEMS are very small, a single device, including contact pads, usually cover $500\mu\text{m} \times 500\mu\text{m}$ space. The samples were diced out of 4 inch wafers. An automated diamond saw was used to ensure that each chip is at the same size. In order to protect the substrate from saw dust, the wafers were coated with a thick layer of photoresist before dicing. An acetone bath after, will strip away to resist make sure that the chips can be removed easily.

2.3 Lithography

Lithography refers to the pattern transfer method invented by Aloys Senefelder in 1796 as a cheap printing method and until 1950s was mostly used for artistic purposes [27]. With the addition of photomasking and chemical processing photolithography was developed. Following this first commercial ICs were introduced in 1961. Pattern transfer methods used in this work are photolithography and electron beam lithography.

2.3.1 Photolithography

Photolithography is the foundation upon which the microelectronics and IC industry is built upon. It is a method of pattern transfer from a photomask to a substrate by exposing organic photo-sensitive materials called photoresist to ultra violet (UV) light. Photoresists are photoactive organic polymers mixed with solvents and when exposed to UV light, undergo a chemical reaction which strengthens or loosens the bonds between their molecules depending on the resist type. If the exposure strengthens, *cross-links*, the bonds; it is a *negative* photoresist whereas if the exposure loosens, due to *chain scission*, the bonds; it is called a *positive* photoresist (Figure 2.3). In this work, positive photoresists were used and for remaining part of this section each photoresist mentioned will be positive.

In order to transfer the pattern, the exposing UV light must be masked by a photomask. For this work commercially available 5 by 5 inches soda lime glass photomasks were used. One side of the glass is coated with 5300Å AZ1500 photoresist on top of 1200Å opaque chromium layer. The design, drawn in a GDSII editor, is then patterned to the mask using a mask writer which is a laser or electron beam lithograph. After the patterning, the photomask is developed in a solution and depending on the photoresist type, positive for this case, exposed or unexposed parts of the photoresist is dissolved (Figure 2.2). Now the exposed parts of the chromium layer can be wet etched by a commercially available chromium etchant while the remaining photoresist act as an etch mask. This process of *mask making*

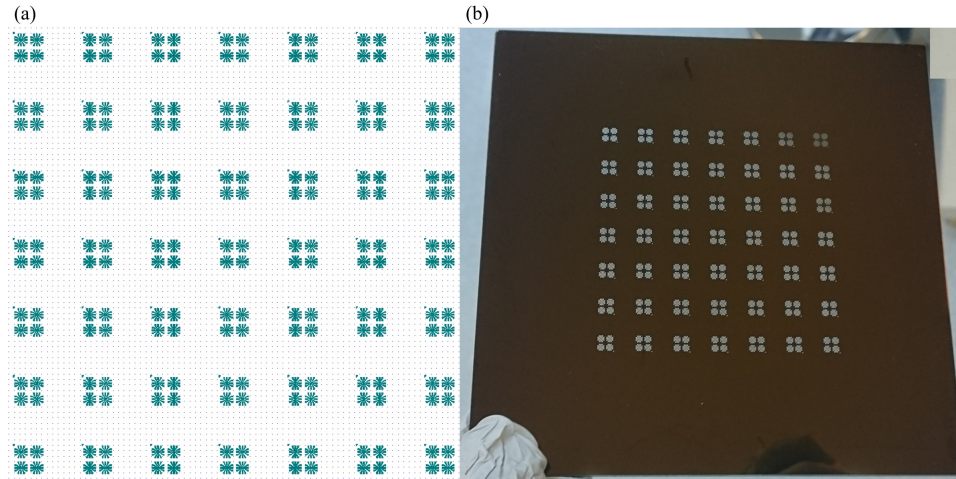


Figure 2.2: GDSII design of contact pads (a) patterned onto a 5 inch soda lime photomask (b) by a mask writer.

is essentially a full fledged fabrication by itself.

2.3.1.1 Spin Coating

Spin coating is a method to coat a substrate with photoresist. Sample is spun at very high speeds (typically 1000 to 6000 rpm) to ensure that liquid photoresist spreads uniformly on the surface. There are other methods of photoresist coating such as spray coating, dip coating and so on.

After sample surface is prepared, it must be baked on a hot plate at 120°C for one minute to ensure there is no moisture on the surface which can affect the adhesion of the photoresist. On some occasions certain photoresists do not adhere well to the substrate surface even after dehumidifying step. In such cases, as an optional step, the surface can be further *primed* by spin coating an adhesion promoter such as Hexamethyldisilazane (HMDS) before photoresist coating. The sample is placed on a spinner and fixed by a backside vacuum. Photoresist is poured on the sample with a plastic pipette. The sample is spun at desired rpm to achieve a certain resist thickness which depends on parameters such as molecular weight, solvent percentage, viscosity. While corresponding thickness can be calculated there are spin curves for each photoresist, available from their

respective manufacturer.

If the surface was not cleaned properly and there are solid particles that are at similar size or larger than the photoresist thickness they will cause streaks. Operator should make sure that during the pouring step no bubbles form on the resist. These imperfections would cause a nonuniform resist thickness which could influence the results of subsequent steps.

After the spin coating, the solvent part of the photoresist does not evaporate completely and could contain built in stresses [27]. In order to evaporate the solvent, the sample must be heat treated. This step, called the *soft bake* or *pre-bake*, can be done by baking the sample on a hot plate, typically 1 minute at 90 – 110°C. The bake temperature and duration depends on the resist type, desired thickness and exposure parameters. The soft baked sample is now ready for exposure.

2.3.1.2 Exposure and Development

Exposure step involves exposing the photoresist layer to UV light while masked by a photomask as shown on figure 2.3. When required, a handheld UV flash light can be used; however, for almost all processes an exposure tool should be used. In UNAM there are mask aligners that can be used for exposure. These tools allow for alignment between different layers and controlled exposure of the samples. There are two main exposure methods for photolithography: shadow printing and projection printing [25]. Projection printing allows for exposure of numerous wafers at the same time allowing high throughput fabrication. In this study proximity printing method was deployed where the photomask is in close proximity to the substrate.

Molecular bonds at the exposed regions are loosened and will be now dissolved by a step called development. Each photoresist have corresponding *developer* which dissolves the photoresist. For positive photoresist, the exposed parts become extremely soluble compared to unexposed parts. Development parameters

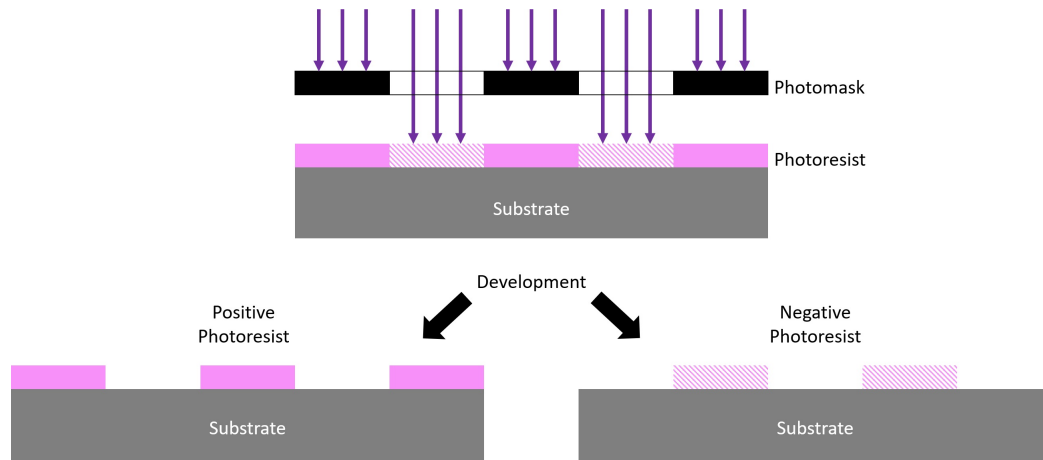


Figure 2.3: Exposure Process and effect of UV radiation on positive resist (a) and negative resist (b).

are determined according to the resist type, resist thickness, and exposure levels. Developer can be diluted with water to decrease the development rate.

Development process involves dipping the exposed sample into a diluted developer for timed duration. After the duration is over, the sample is rinsed with DI water immediately to stop any remaining developer to further react with resist. At this step optical microscopy should be used determine the success of development. If the exposed photoresist did not dissolve completely (underdevelopment), a subsequent development can be applied. On the other hand, if the development was too much: process duration could be decreased, developer can be further diluted or the exposure dosage can be lowered.

After development, sample is usually *hard-baked* to ensure even better adhesion between photoresist and sample surface by evaporating any remaining solvent. If material will be deposited on top of the photoresist, typically 30-60 seconds bake on a 110°C hard plate can be applied. If the resist is going to be used directly as an etch mask, even longer bakes at higher temperatures must be applied to further strengthen the resist. Either way this is the last step of a typical photolithography process.

2.3.2 Electron Beam Photolithography

Electron-beam lithography (EBL) is a high resolution direct writing method. Direct writing refers to the fact that there is no need for a mask in order to transfer a pattern. Instead of UV light, focused electron beams (e-beam) are used for exposure. Thus EBL is not limited by the diffraction of light and can be used to pattern sub 100 *nm* features. Electron-beam sensitive resists (e-beam resist) are used as a substitute to photoresist. Other than these differences EBL process steps are similar to photolithography.

There are two types of EBL setups. First type is essentially a modified scanning electron microscope (SEM) where the SEM is converted with an appropriate pattern generator hardware and software to an EBL. The other types are standalone EBL with automatic stitching and marker detection features. The EBL used in this MS study was one of the former, a FEI SEM that is converted to an EBL by a RAITH pattern generator module which manipulates the magnetic coils and beam blanker that turn on and off the beam to direct the beam to different points on the sample.

Even though state-of-the-art photolithography techniques, i.e. extreme UV lithography, are able to reach similar features sizes as EBL; they need very expensive devices and are not cost effective without fabricating thousands of devices with each batch. For research purposes and prototyping, where high throughput is not necessary, EBL offers a cost effective replacement for writing linewidths smaller than 1 μm . Even though EBL is mostly used for mask writing in the industry, it has become an indispensable tool for research oriented fabrications.

2.3.2.1 E-beam Resist

Poly(methyl metacrylate), PMMA for short, is a commonly used e-beam resist. Similar to photoresists, e-beam resists are polymers mixed with certain solvents to modulate viscosity and resist thickness. For instance, PMMA A4 495k is an e-beam resist frequently used in this work. In this case, 495K refers to the fact that

this PMMA has a molecular weight of 495 *kDa*. A4 means, PMMA is dissolved in anisole and solid contents in this resist are 4% by weight. Anisole can also dissolve plastics; thus a glass pipette should be used when pouring this PMMA on substrates.

E-beam resists, like photoresist, can be spin coated on the substrate. Spin curves are available from manufacturers. Due to the feature sizes involved are smaller than photolithography e-beam resist layers tend to be much thinner compared to photoresist. As a result, e-beam resists are not very suitable as hard etch masks. While lift-off is relatively easier for EBL due to inherent undercutting, a bilayer resist can be applied to achieve even more pronounced lift-off geometries. A higher molecular weight resist is coated on top of a lower molecular weight resist which requires a lower electron dosage for dissolution, resulting in a better undercut after development [32]. A commonly used bilayer e-beam resist recipe (Table 2.1) used in this work results in 300 *nm* PMMA thickness.

Due to electron penetration, the minimum feature size of EBL is affected by the resist thickness. A rule of thumb for 30 *kV* electron acceleration is: the resist thickness should not be more than 3 times the desired minimum feature size. For instance for 100 *nm* features, the resist must not be thicker than 300 *nm*.

Table 2.1: PMMA bilayer spin coating recipe for 300 *nm* thick film.

1-	10 minute bake on hotplate at 180 °C
2-	PMMA 495K A4 at 2000 RPM for 40 seconds (215 <i>nm</i> resist thickness)
3-	5 minute bake on hotplate at 180 °C
4-	PMMA 950K A2 at 3000 RPM for 40 seconds (80 <i>nm</i> resist thickness)
5-	10 minute bake on hotplate at 180 °C

2.3.2.2 Exposure and Development

Instead of UV light, EBL uses an e-beam to expose the resist. Generated electrons are charged by electrostatic fields up to 100-200 *keV* then the beam is focused and narrowed by a system of magnetic lenses and apertures [32]. The current of the e-beam can be measured by a Faraday cage on the stage that is connected to

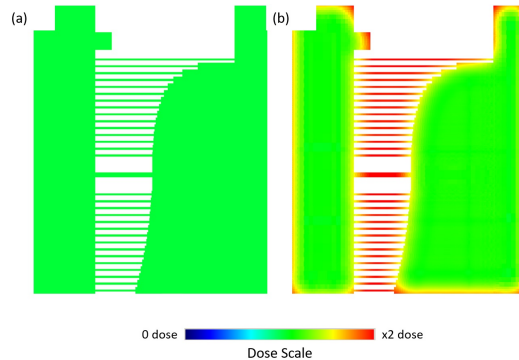


Figure 2.4: Dose factors for the same design. (a) has no proximity correction while (b) is proximity corrected.

a multi-meter. Since EBL is not limited by the diffraction of light, it possible to achieve smaller minimum feature sizes down to few tens of nanometers. However, the feature sizes are limited by electrons scattering into the resist and back-scattering from the substrate [25].

The lateral scattering also causes an issue called *proximity effect*. Since the exposed areas are larger than the spot size, due to scattering, the neighboring patterns affect each other. Thus, correction is required to calculate optimum exposure dosage at local patterns. These corrections are called proximity correction which depend on the resist type, resist thickness, substrate type, and e-beam voltage and current. These corrections requires cumbersome calculations; fortunately, there are pre-calculated corrections available for commonly used substrates and resists. In this work corrections available from RAITH EBL software library were used.

On figure 2.4a, dose factor is same for each part of the design. In this case, the smaller beam like structures in the center would not receive enough dosage while the large clamp areas do not require as much dose since the exposed are is large. Furthermore, centers of those beam would be thinner than the base of the beams affecting the geometry. Figure 2.4b is the corrected version where smaller features and edges receive higher dose and central parts of larger geometries receive less.

The dose parameters must be calculated according to the desired dosage and

electron beam current. For the EBL setup used in this work, the beam speed should not exceed 10 *mm/s* since magnetic coils do not work properly at higher beam speeds.

Development step is very similar to photolithography. Exposed sample is dipped in developer for a certain amount of time to dissolve exposed parts of the resist. A common developer used for PMMA is Methyl isobutyl ketone (MIBK). Typical PMMA development process can be seen on table 2.2.

Table 2.2: PMMA development procedure.

- 1-** 1 minute dip in MIBK:IPA(1:3) solution
- 2-** 5 seconds MIBK:IPA(1:1) dip.
- 3-** 30 seconds IPA dip to stop the reaction.
- 4-** N₂ drying.

2.3.2.3 Dose Test

EBL is a very complex fabrication step with numerous parameters from resist thickness to electron beam current that severely affect the process outcome. Thus, before starting a new design a dose test must be done. Operator must ensure that each test sample has same thickness of resist and has gone thorough identical procedures. Design must be patterned on to the test sample at separate locations, with sufficient distance and varying exposure doses. After development, the specimen must be characterized with an SEM to analyze and decide on the optimal dosage. Operator must be swift and use the beam blanker during the imaging process as SEM imaging is essentially electron bombardment of the sample and further exposure occurs. Although it is time consuming and not necessary at all, an optional metallization followed by lift-off can be applied to the dose test samples. This way, the patterns will not be affected by the SEM imaging and the characterization could actually give more information.

A typical example of dose test is shown on figure 2.5. A design is patterned with increasing doses, developed and imaged with SEM. If the dose was not sufficient, PMMA will not develop properly (figure 2.5a). On the other hand if

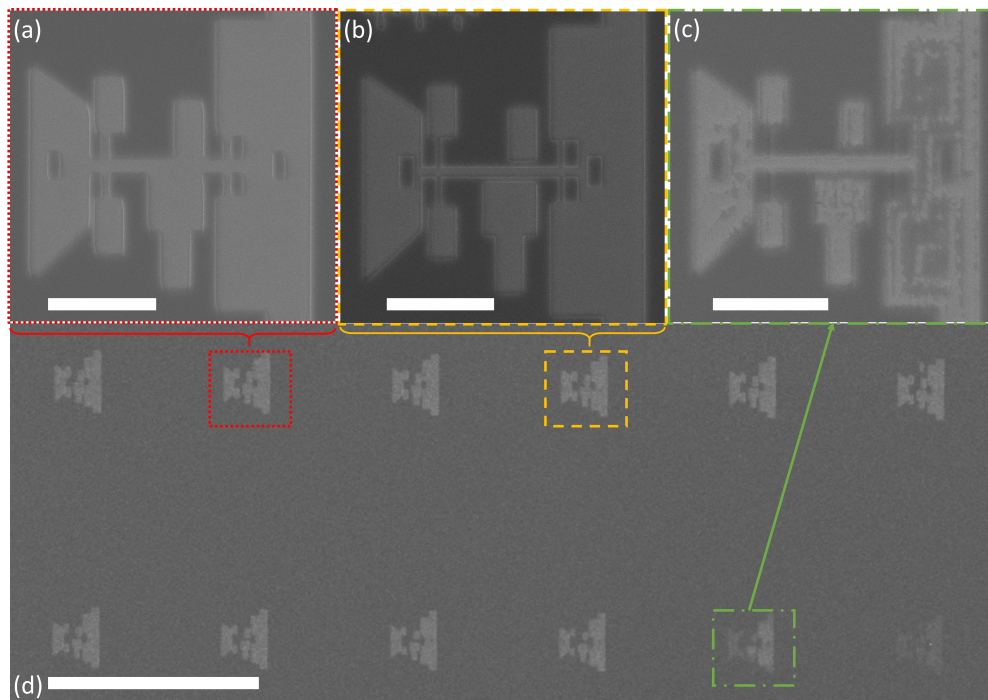


Figure 2.5: Dose test characterization by SEM. 10 identical design with varying dose factors (d) were patterned. Closer examination shows: overexposure (a), optimal dose (b), and underexposure (c). Scale bars are $4 \mu m$ for top row images and $50 \mu m$ for (d).

the exposure is too much the electrons will scatter farther and the unintended parts of the resist will develop (figure 2.5c). Using small enough increments it is possible to locate an optimal dose (figure 2.5b) with closest dimension to the design. Development duration can be also altered to control the features sizes. After an acceptable dose is determined, the operator can use the settings to pattern the actual samples.

2.3.2.4 Alignment

Alignment is a process that allows for the EBL software to recognize a position on the physical plane of the stage and align those markers to the design plane. It works by moving to alignment markers that are either patterned before or are a part of the bare substrate. E-beam is controlled with magnetic coils; consequently, the writing area, *writefield*, is limited. If the design is larger than the maximum writefield possible, it cannot be patterned with one step. Furthermore, most of the work done in this study involved patterning of more than one layer which requires the sample to be taken in out of the chamber more than once. In such cases an alignment procedure must be done to stitch larger designs or different layers. While automatic marker detection was possible within the RAITH software, SEM column limited it to manual marker detection. Therefore alignment procedures were the most tedious and time consuming part of the fabrication.

Markers should be easily identifiable and distinguishable, especially when there is more than one alignment step. Further, the markers should be large enough to accommodate stage errors. Figure 2.6 shows the initial locations of marker scans in green. Even though the scans are not precisely on top of the markers, small part of the markers are still visible. If not, the operator could not align at all. This scan procedure exposes the resist and these locations gets deposited. Therefore the marker locations should be far enough from the device features.

Since the mechanical stage of the EBL had an error of $10\ \mu\text{m}$ for $100\ \mu\text{m}$ lateral step, there was a need for alignment after each time the stage moved. For electrothermally actuated NEMS fabricated in this work, the error tolerance was

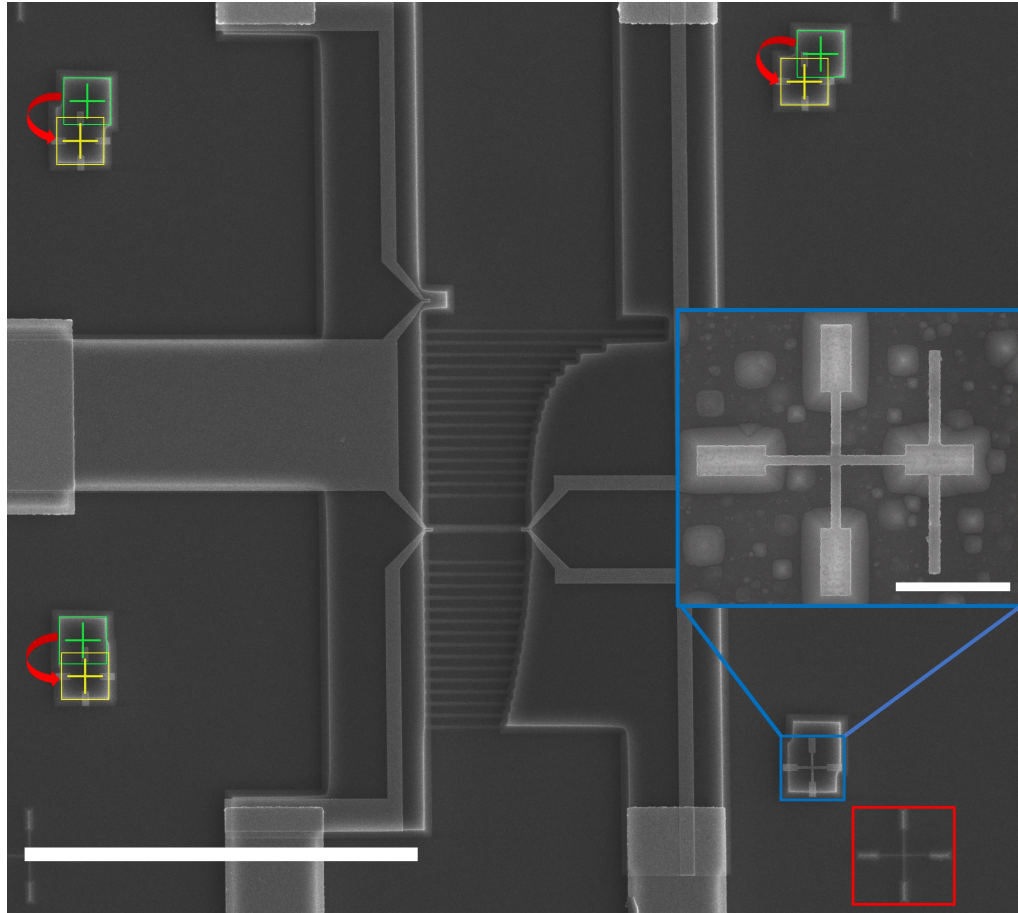


Figure 2.6: SEM image of a NEMS device that had gone through 2 alignment procedures. Green cross-hairs marks the initial point of the marker scans and yellow cross-hairs the aligned position. Red box shows one of the markers of the alignments step for the previous layer. Inset shows a closed up view of an alignment marker. Scale bars are $40 \mu m$ and $4 \mu m$.

50 nm . A comprehensive checklist to operate Raith Elphy Plus EBL software during alignment procedure can be found on appendix B.

2.4 Evaporation

Evaporation is a subset of physical vapor deposition, a commonly used thin film deposition method that can be separated into two groups: physical vapor deposition (PVD) and chemical vapor deposition (CVD). “CVD essentially involves the

process of dissociation of molecules of the gaseous reactants, which subsequently react chemically to form various structures when activated by heat, light, or plasma discharge” [24]. In PVD, on the other hand, the target material is heated up and goes under a physical state change. While it is mostly used for metal deposition some semiconductors and oxides can be deposited as well. (Si, Ge, SiO₂, TiO₂, etc.) Some examples of PVD methods are as following: sputtering, molecular beam epitaxy, ion plating and, so on. However this work will focus on evaporation.

Evaporation is done in a vacuum chamber so that the atoms in vapor can directly move toward the substrate and strike the surface to form a thin layer [26]. If there is not a sufficient vacuum, the atoms in the vapor would collide with atoms present in the chamber and might not reach the substrate surface. Even if it does reach the surface, the particles in the chamber atmosphere could stick to the vapor; which would contaminate the deposited layer. Therefore, the pressure must be at the levels at which the mean free path of the molecules are larger than the distance between the target material and the substrate surface. Evaporation should be performed at pressures around 10^{-6} Torr [22]. In order to achieve these pressure levels, a rough pump accompanied by a turbo molecular pump, or an oil diffusion pump must be used.

The thickness of deposited films can be monitored by thin-film thickness monitors. Usually a quartz crystal micro-balance is used as the sensor. *Rate monitor* is placed to a close proximity to the substrate. When the material is being deposited on the substrate, because of the close proximity, the crystal will be also covered with the deposited materials. By tracking the resonance frequency of the crystal, which will decrease with the deposition of new material due to added weight, it is possible to measure the film thickness. Since there would be an inevitable difference between the amount of material that strikes the substrate and the crystal a calibration must be made. These calibrations, although can be calculated very precisely, usually are done empirically. Typical parameters of a thickness monitor are: Tooling factor, material acoustic impedance and material density. After certain amount of usage the crystal must be changed as its sensitivity will decrease. The operator should make sure to track the crystal

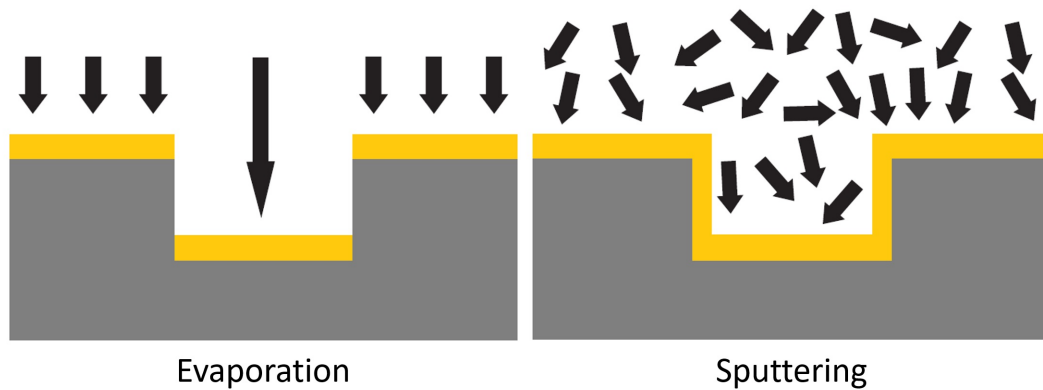


Figure 2.7: Step coverage of evaporation and sputtering. Adapted from [33].

lifetime.

During the deposition, substrate temperature will increase since target material is heated to its melting point. Moreover, the deposited film will be very hot. If the vacuum is breached immediately, the room temperature atmosphere could cool down the thin layer very rapidly which could cause the film to buckle under these quick changes in thermal stress. In order to prevent this, the substrate should be allowed to rest for 15-20 minutes under vacuum before braking it.

Because of this “ballistic” [26] deposition, where the atoms in the vapor strike directly to the substrate surface, there is an issue of *step coverage* with evaporation methods (Figure 2.7). In order to overcome this limitation substrate rotation and heating could be applied. Or another thin film deposition method sputtering could be used when step coverage is required for the fabrication process. However, step coverage can be detrimental for lift-off purposes, which will be covered in the next section. Thus, this limitation in step coverage was actually desired for this study.

2.4.1 Thermal Evaporation

Thermal Evaporation is an additive pattern transfer method that utilizes DC electric current to heat the target material to its melting point to deposit the

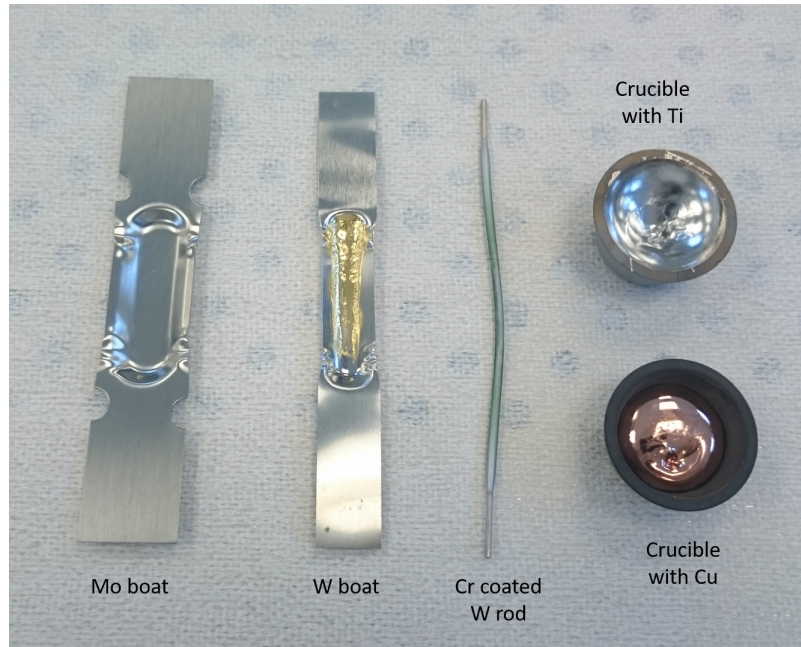


Figure 2.8: Few example of boats and crucibles used for evaporation.

material onto the substrate. Figure 2.9 shows inside a thermal evaporator chamber. In thermal evaporation, target material is put in to a metallic *boat*. As high current passes through the boat (figure 2.8), typically around 100 A, both the boat and target material heats up. While there is always an equilibrium of vapor pressure above the material [26]; in order to achieve reasonable deposition rates the target material is heated up until molten state. Obviously, the melting point of the material should be lower than the boat itself or the boat will melt and the evaporation process will fail. With thermal evaporator, it is possible to deposit materials with melting point up to 1800°C. For materials with lower melting points, such as Au and Ag, molybdenum boats are used. For higher melting points, i.e. Cr, tungsten boats are more suitable as molybdenum boats would fail. There are also rods coated with evaporation material available. In this work chromium coated tungsten rods were used for chromium deposition (Figure 2.8).

During thermal evaporation it is important not to change the current passing through the boat rapidly. First of all, sudden changes in temperature can break the boat and stop the whole procedure. Moreover, it can affect the thin film uniformity if the deposition rate keeps changing. Additionally, initial deposition

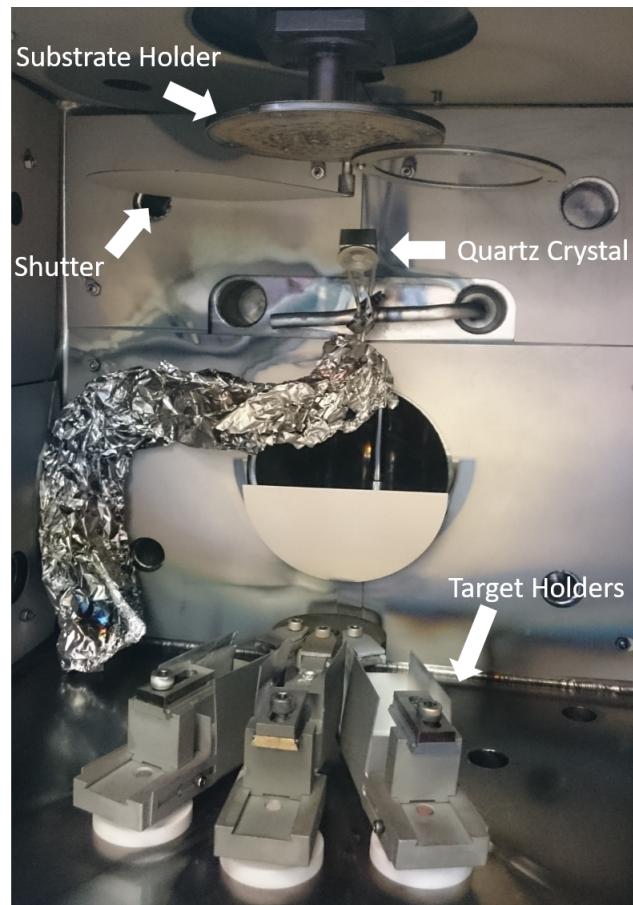


Figure 2.9: Inside of a thermal evaporator chamber. This particular thermal evaporator has three target holders which can be used subsequently for layer by layer deposition or simultaneously for alloy deposition.

rate must be very slow to ensure adhesion to substrate. The first few nanometers would acts a seed layer and rate could be increased after. It is good practice to start with $0.1\text{\AA}/s$ for 2 nm and then increase the rate. Usually passing $1\text{\AA}/s$ is not advised for thermal evaporator. However, e-beam evaporation is not affected by this $1\text{\AA}/s$ limit as crucibles are much more sturdy than boats.

2.4.2 Electron Beam Evaporation

For materials with higher melting points, an e-beam evaporator can be utilized (Figure 2.10). Instead of a DC electric current, a magnetically steered [26] electron beam, typically around 10 kV , is used to heat up the target material. Crucibles are used for e-beam evaporation which are placed in water cooled hearts to accommodate the high temperatures. Another advantage of e-beam evaporator is the higher deposition rate due to the higher temperatures can be reached with electron beam. In this work, e-beam evaporator was used for copper etch mask deposition. While thermal evaporation could also be used to deposit copper, the deposition rates are much slower than the e-beam evaporation.

2.5 Lift-off

After lithography process, a thin layer can deposited on to the substrate to fill the patterns. To complete the pattern transfer, a method known as *lift-off* must be applied. The sample is soaked in an acetone bath for 6 or more hours, depending on the feature sizes, to strip away the resist and the deposited material on top of it. For NEMS device layers in this work, overnight lift-off was used to ensure proper lift-off. At this time the lid of the bath should be sealed to ensure that acetone will not evaporate completely. Failure to prevent acetone evaporation could cause in a failed lift-off; moreover, solvents should never be allowed to evaporate on substrate surface normally.

Exposed and developed substrate (Figure 2.11 a) is dipped into an acetone bath

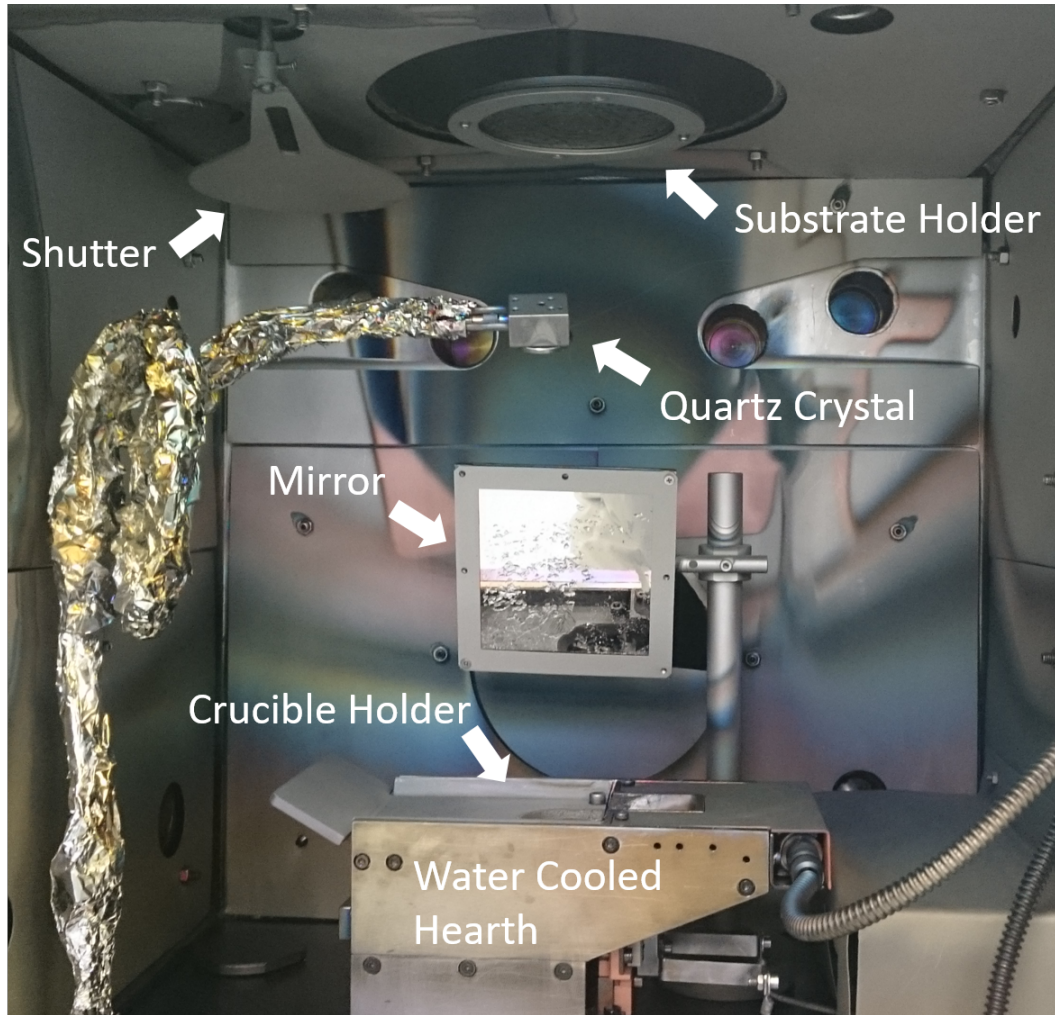


Figure 2.10: Inside of an e-beam evaporator chamber. Target material is put in a crucible that goes to the crucible holder which sits on top of a water cooled hearth. The mirror is used to visually track the electron beam which should be directed on to the crucible. This particular e-beam evaporator can hold four crucibles at the same time but does not allow for simultaneous deposition.

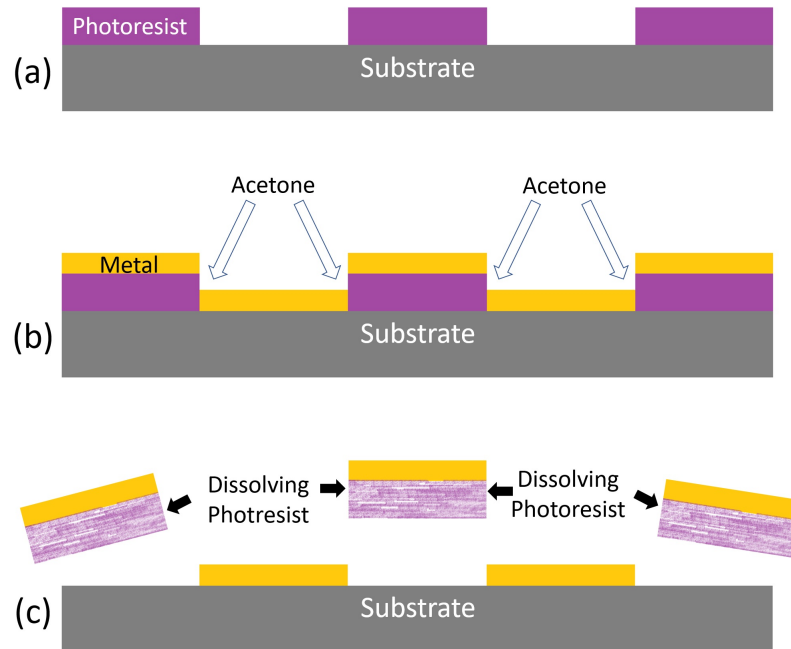


Figure 2.11: Lift-off mechanism.

after metallization (Figure 2.11 b). Acetone starts to dissolve organic photoresist where it can reach it. Dissolving photoresist strips away with the metal layer on top of it (Figure 2.11c). After the process is over; the sample should be put in a sonic bath for a short duration, typically a minute, to strip away any remaining resist. However, this sonic bath should not be overdone or the deposited thin layer could be stripped away as well. If done correctly, the desired pattern is now transferred on to the sample.

For a successful lift-off, the thumb of rule used for this work was the 1 to 3 ratio. The resist thickness should be at least 3 times thicker than the deposited material in order to ensure a successful lift-off, especially for submicron structures. Otherwise, acetone might not seep through the crevices between deposited layers and resist. This a very important rule to follow especially for submicron features as acetone has to physically reach the underlying resist. This is the reason why for a lift-off process the step coverage is not really desired as it would prevent acetone to reach underlying resist. The 1 to 3 ratio rule is more flexible with larger feature sizes. Figure 2.12 shows two examples where 3 to 1 ratio was not

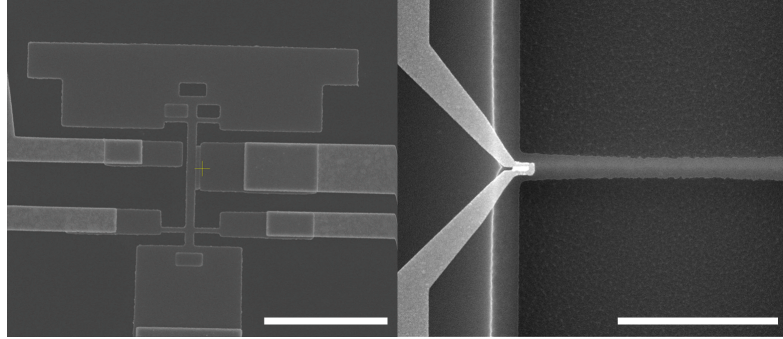


Figure 2.12: Examples of unsuccessful lift-off procedures. Both scales bars are $5\ \mu\text{m}$.

followed and the lift-off was unsuccessful as acetone could not seep into small features.

2.6 Etching

Etching is a subtractive fabrication method where materials which are not protected by an *etch mask*, are stripped away either chemically, physically or with a mixture of both. After the lithography step, a sample can go through etching process directly or another step of thin layer deposition or oxide growth might be applied before etching. There are two types of etching: wet and dry.

2.6.1 Wet Etching

In wet etching, the sample is dipped into a liquid solution, called etchant, that would react with sample surface. In some cases vapor of the etchant can be also applied. Wet etching mechanism involves three steps: reactants in the etching solution reaches to the surface, chemically reacts with substrate surface and the products from the reaction are removed by diffusion [25]. The removal rate from the surface is deterministic for the etch rate. This diffusion can be controlled by the temperature of the etchant. Physical removal of byproducts also affect the etch rate, for example stirring the solution.

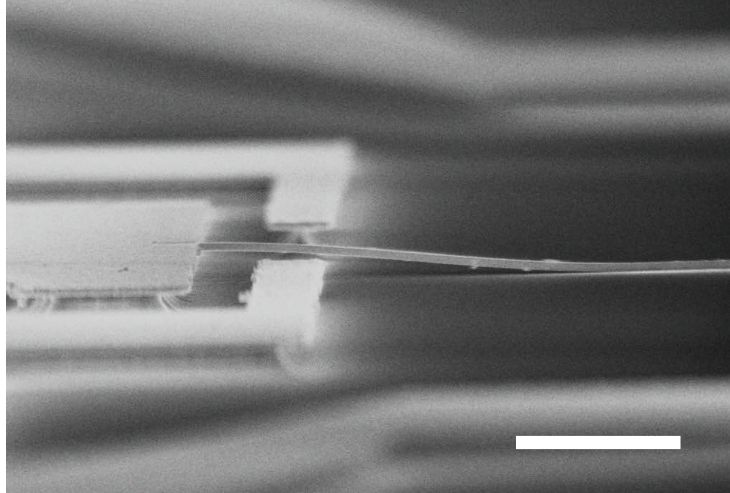


Figure 2.13: Stiction of a silicon beam after HF based oxide wet etch. Scale bar is $5 \mu m$.

One of the biggest disadvantage of wet etching is the *stiction* caused by the liquid meniscus left under suspended structures during drying (Figure 2.13). This liquid pocket pulls the structure to the substrate surface with capillary forces as it evaporates. After the evaporation, suspended structure might stick to the surface due to the strength of Van der Waals forces at small scale. This is especially critical for cantilevers and very long and thin features. To overcome this issue a critical point dryer can be utilized.

Wet etching is highly selective due to its chemical nature. Moreover, etch isotropy is affected by the crystal structure of the material. However, for shallow etches, under $1 \mu m$, it is hard to time the etch correctly since etch rates are relatively higher compared to dry etch. In this work, wet etching was used to strip away metallic dry etch masks.

2.6.2 Dry Etching

Dry etching is a subtractive method where solid surfaces etched by a gaseous species. *Dry* refers to the fact that in no step of etching, the sample comes into contact with wet chemicals. This eliminates any stiction problem that may

occur. Moreover, especially with submicron features, wet etchants sometimes cannot seep into every crevice whereas in dry etching gaseous molecules can move more freely. Dry etch can be physical (ion bombardment, sputtering), chemical (radical) or both physical and chemical (reactive ion etching (RIE)) [27]. In a purely physical etch, (i.e. ion milling) inert species, such as Ar, are directed to the substrate surface with high energy, dislocating the atoms. In radical (chemical) dry etch, the ionized reactants form molecules with the substrate atoms and these volatile compounds are then pumped away. RIE, by combining both reactive (chemical) and nonreactive (physical) gasses together utilizes the selectivity of the chemicals and anisotropy of the high energy ions.

Dry etching uses gas or vapor plasma created by an electric field to etch the substrate. This plasma can be created with DC, AC (50 kHz and up), RF (13.56-27 Mhz), or microwave fields (300 MHz and up). When an electric field with sufficient magnitude is applied to the gas, free electrons oscillate and collide with gas molecules ionizing them [25] creating a *quasineutral* plasma which has equal number of positive and negative charges. This high energy reactive plasma then reacts or collides with the substrate surface.

In this work, plasma was created at RF frequency by an inductively coupled plasma (ICP) device. In the upper part of the chamber a coil operating at 13.56 MHz (communications standard) drives the plasma inductively and creates a low pressure, low energy, and high density plasma (figure 2.14) while the 13.56 MHz platen at the bottom of the chamber modulates the ion bombardment energy [27]. The substrate then gets bombarded with ions, reacts with the plasma which etches the sample.

Selectivity is an important parameter of etching as it is a measure of etch rate ratios between a target material being etched and the masking material. The mask could be either a deposited thin film, a layer of grown oxide, or a photoresist. In order to etch targeted locations and mask the others, there must be enough selectivity between the materials. For example 100:1 selectivity between a target material and mask would mean that 100 unit of the material is etched by the time 1 unit of mask material is etched. Higher selectivity is desired for an etch but in

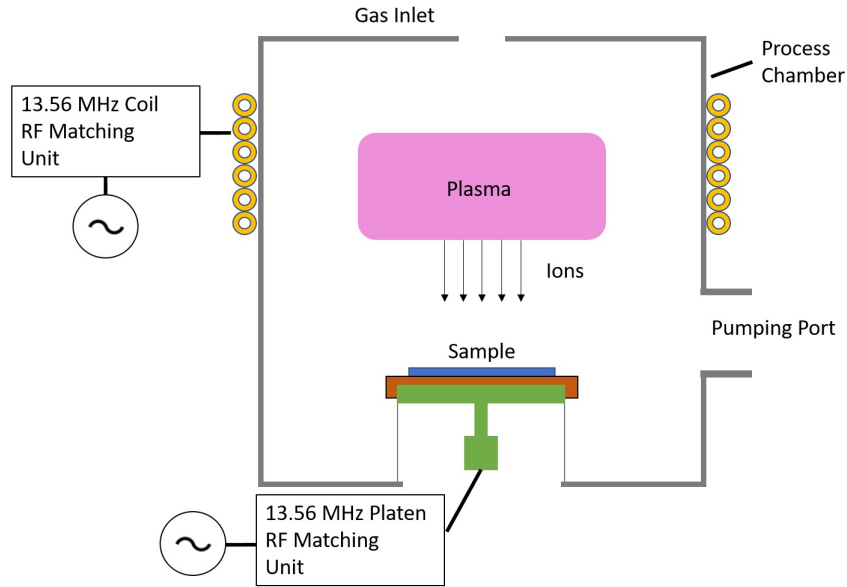
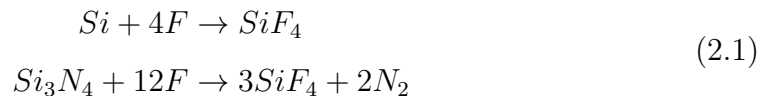


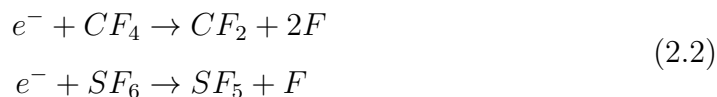
Figure 2.14: Schematic of an ICP chamber. Adapted from [34].

some circumstances a thicker mask can circumvent this need. After many tests, e-beam evaporator deposited Cu etch mask was used in this work. It is highly resistant to fluorine based etch and can be removed easily with a commercially available aluminum etchant.

In this study, RIE of silicon and silicon nitride was utilized. Etch mechanism depends on many parameters. First of all the selected etchant species should react with substrate. For silicon and silicon nitride, fluorine based etches are quite common resulting in volatile SiF_4 by products. The chemistry is as followed [32]:



Free fluorine can be generated by fluorinated gasses. CF_4 and SF_6 ionization is given by [32, 35] :



In this work, the goal was to suspend silicon nitride doubly clamped beams on sacrificial silicon layer. In order to achieve this, silicon nitride must be etched first. To achieve a prismatic beam geometry with perpendicular side walls the etch must be anisotropic and the undercut should be minimized. Increasing the ion bombardment energy by biasing is one of the most influential way to achieve better anisotropy. Additionally, using inert molecules, such as Ar, will increase the anisotropy. However this method result in heavy ion bombardment of the substrate and requires a very strong and thick mask. Yet, the feature sizes of our devices did not allow mask thickness more than 100 *nm*. Moreover, the substrate surface could be damaged by these high energy ions.

Another option is to inhibit the reaction by coating the substrate with a polymer. This is called wall passivation. By adding fluorocarbons (i.e. CHF₃, C₄F₈) to the gas mixture, polymerization on substrate surface can be achieved which will block the reactions. Although polymerization occurs both on vertical walls and horizontal surfaces, the high energy ions in the plasma will quickly etch the horizontal surfaces; yet, the vertical walls will not be affected by these ions as the electric field does not direct the ions on the walls. Wall passivation is an important aspect of RIE and was very critical for the development of deep RIE which is used to etch hundreds of microns deep into silicon substrates. Thus, a recipe based on CF₄ as free fluorine source with additional wall passivation was used. In order to etch silicon isotropically, SF₆ was used. CHF₃ was also added to protect the silicon nitride device layer. Etch recipe and ICP parameters for these two process is given on table 2.3.

2.6.2.1 Recipe development

Recipe development was an important and time consuming part of this study. While selectivity of many materials and corresponding etch mask could be found

Table 2.3: Etch recipes developed for silicon nitride and silicon for STS ICP.

Recipe	Anisotropic Si ₃ N ₄	Isotropic Si
Etchant Flow (sccm)	20 CF ₄	15 SF ₆
Passivation Flow (sccm)	3 CHF ₃	2 CHF ₃
Coil Power (Watt)	400	150
Platen Power (Watt)	100	30
Pressure (mTorr)	5	10
Temperature (°C)	25	25
Duration (Min)	1	4

readily in the literature [36], they do not always work exactly the same. Although etch recipes should be always modified and tuned for individual etching systems, the first step should be a literature review. There are many considerations: etch isotropy, reactivity of the substrate, selectivity of potential mask materials, availability of certain gas plasma, removability of the etch mask and so on.

After the literature research, possible etchants and mask should be selected. Small but numerous samples should be patterned and etch masks must be deposited. Starting with parameters found from literature, the samples must be etched. After each etch there should be extensive characterization to analyze the etch. According to the results the parameters should be tweaked. If the etch rate is too slow the coil power can be increased. If sidewall angles are not perpendicular enough platen power can be increased or pressure could be dropped to increase anisotropy. In some instances etchant gas could be changed altogether if chemistry does not work with the substrate.

During this work many etch tests were done in order to find optimal recipes. Figure 2.15a shows typical step of recipe development occurred for this study. Anisotropic etch of nitride device layer resulted in vertical side walls thanks to the high coil and platen power and also added CHF₃ passivation (Figure 2.15a). Figure 2.15b shows result of an initial silicon isotropic etch trial. Etch seems isotropic by judging the underetch yet the beam is not suspended. In this situation there are few options: temperature can be increased to increase chemical reaction, SF₆ gas flow or coil power can be increase, or simply the etch duration

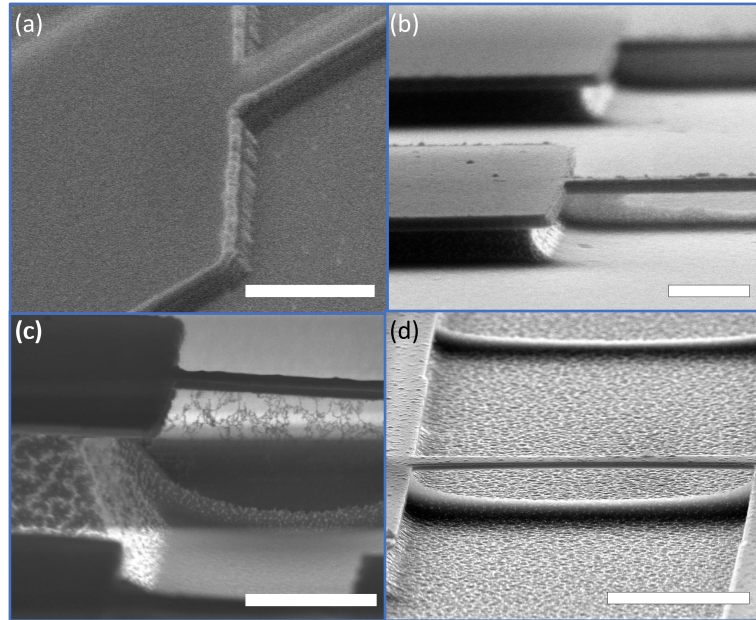


Figure 2.15: Etch recipe development steps. Scale bars on top row are $1 \mu m$, (c) $2 \mu m$ and (d) $3 \mu m$.

can be prolonged. After appropriate corrections done another trial is made (figure 2.15c) and characterization shows a web like structure under the beam. Even though no further characterization was done to prove it, it was assumed to be the CF_x fluoro carbon plasma polymerization [37]. Further etch did not remove it. On the other hand, it shows that wall passivation does work. However, it must be removed to suspend the beam. Thus, the CHF_3 gas flow was reduced and another etch step was resulted in the fully suspended beam shown on 2.15d).

2.7 Wirebonding

Wirebonding is often the last step of fabrication and is used to connect the small contact pads of micro devices to outside world. Since the contact pads are very small for soldering, a very thin spools of metal wire is used to connect these pads to printed circuit boards. The wires have a diameter of approximately $30 \mu m$. Bonding can be done by two methods; ball and wedge bonding. In ball bonding first a small spark melts the tail of the wire which forms ball at the end of a

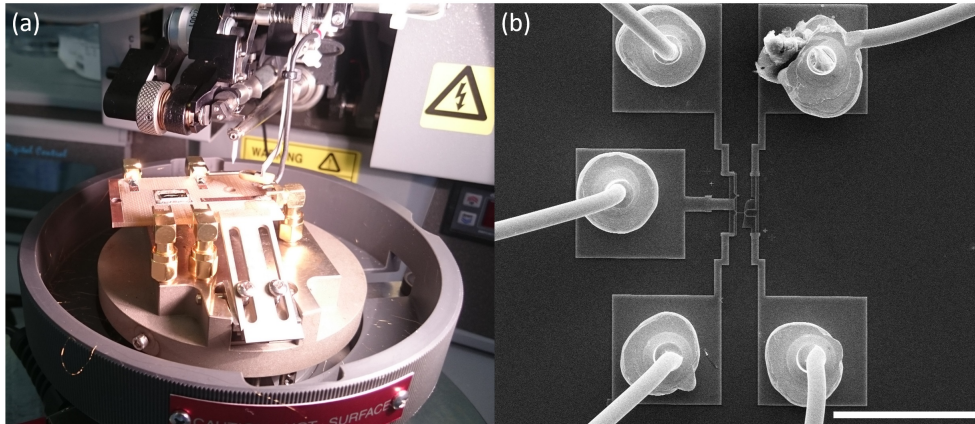


Figure 2.16: Photograph of a wirebonder during bonding operation (a). SEM micrograph of a wirebonded device (b). Scale bar is $200 \mu m$.

ceramic tip. Operating the wirebonder through an optical microscope the tip is then contacted with the first surface to be bonded. After the ball is squeezed and bonds to the surface, the tip is brought to the other surface of interest and this time is wedge bonded. Ball bonding is essentially a ball-wedge bonding. On the other case of wedge bonding, both bonds are made by wedge bonding. There are parameters of the device such as the force of the tip and time of the contact which can be adjusted for different bonding surfaces. The process, when done manually, is very meticulous and requires a certain thickness of metal to stick reliably. In our experiments we found that bonding to a gold thin layer is very difficult under 100 nm of thickness.

2.8 Characterization

Characterization is a crucial part of any microfabrication process. In industry rigorous quality control at each step of the fabrication utilizing characterization tools has been established. For research oriented fabrications, characterization is might be even more essential since developing new recipes for fabrication requires extra caution. There are many characterization methods that measures different properties of a sample. The characterization can give information about the topography, thickness, composition, electrical, and chemical properties of the

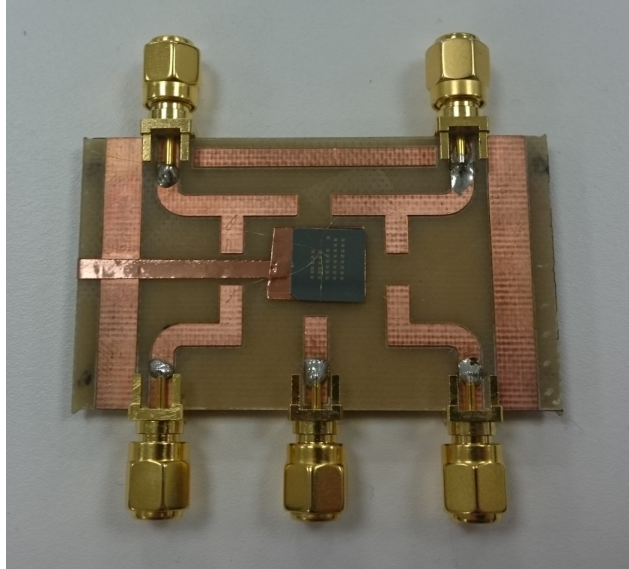


Figure 2.17: A silicon chip with dozens of NEMS, wirebonded to a 5 port printed circuit board.

sample. For example many spectroscopy methods (XRD, XPS, RAMAN, etc.) can be used to determine the composition, physical properties of a sample. These methods are mostly used in tandem with bottom-up fabrication methods were new substrates are grown. Most of these characterization methods are redundant for top-down methods such as the fabrication of this study. In this work optical and scanning electron microscopes were utilized frequently. A stylus profilometer was also used before and after any additive or subtractive step. A probe station was also used to determine resistivity of the transducers.

2.8.1 Microscopy

Optical microscopy, due to the wavelength of light, has a resolution at micrometer range. It is very easy to operate and requires none to very little sample preparation for a fabrication specimen. Other than the common bright-field microscopy; dark-field microscopy can be used to detect steps and edges that reflect light, fluorescence microscopy can be utilized to resolve organic residues and differential interference contrast microscopy is suitable to gather surface-height difference information [26].

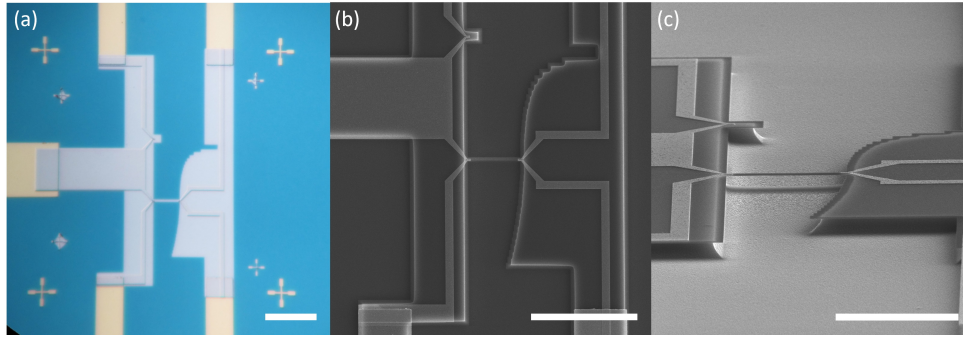


Figure 2.18: Images of a NEMS taken with optic microscopy (a), SEM (b) and tilted view with SEM (c). Scales bar are for (a) and (b) 20 and for (c) 10 μm .

One of the most important tools for microfabrication is the Scanning Electron Microscope (SEM). SEM is not limited by the diffraction of light since it uses scattered electron beams to image and offers resolutions down to few nanometers. The strength of SEM for microfabrication shows in tilted or cross-sectional view. Its high resolution allows to obtain topographic information about layers. However, SEM requires a lot more sample preparation than optical microscopy. Imaging occurs in a vacuum, typically around 10^{-4} bar and lower. Sample must be a solid and if it is not a conductor or semiconductor, it must be coated with a thin layer of conducting material (usually gold or platinum) to prevent charge build up. For cross-sectional imaging often the sample must be diced in half, effectively destroying the sample.

2.8.2 Profilometer

Profilometer is a device used to measure thickness of a thin film by physical or optical means. An optical profilometer uses light to determine thickness of a thin film. The detection could be by optical interference, focus and phase detection, confocal aperture, etc. Since only light is used, it is a non-contact method.

A Stylus Profilometer is a low resolution AFM essentially. It uses a metal tip with a sharp edge to measure the hills and trenches on a substrate. It is a very crucial and practical device for measuring etch rates between etching steps.

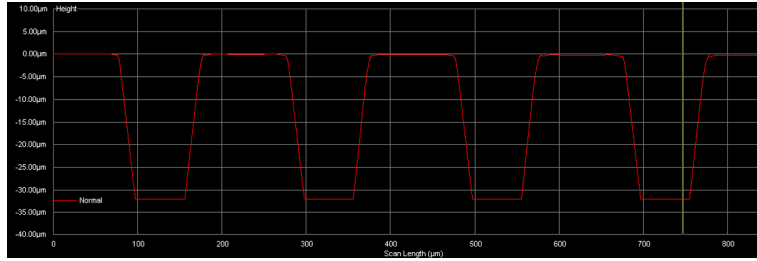


Figure 2.19: Stylus profilometer measurements of sample undergone a 100 cycle DRIE etch showing μm deep trenches.



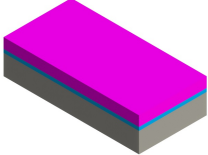


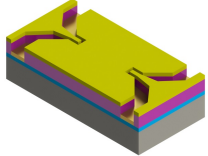

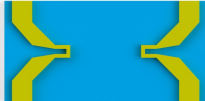
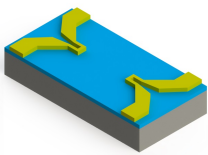


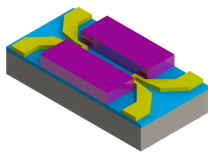
Since it is a contact technique it is not very suitable for soft surfaces and even can be destructive to some. Stylus profilometer uses a feedback system for tip that controls the force applied on the tip, thus it extremely sensitive. Since its a very quick and relatively simple measurement compared to an SEM characterization it was a crucial equipment for developing etch recipes.

2.8.3 Probe Station

Probe station is a semiconductor characterization device that allows for quick analysis of a substrate electrical properties. It consist of a measurement instrumentation and small probes with very sharp needles where the substrate is contacted. Probe station's main purpose is to test electrical features of semiconductors without having to bond the device. It can be also used for 4 probe measurement of a semiconductor resistivity. For this work probe stationed was used to determine resistance of metallic loops without wirebonding the substrate itself.

2.9 Fabrication Steps of Silicon Nitride Devices

A step by step fabrication process of electrothermally actuated and piezoresistively detected NEMS is given on figures 2.20 and 2.21.

Top View	Side View	Isometric View	Process Step
			Commercially available 100 nm thick low-stress silicon nitride grown on top of silicon substrate. Diced and RCA cleaned. 300 nm thick Bilayer PMMA spin coated.
			Contact pads and electrodes are patterned using EBL, developed and followed by thermal evaporation of 100 nm thick Au with 4 nm of Cr adhesion layer underneath.
			After an overnight lift-off the electrodes are patterned onto the silicon nitride device layer.
			A new layer of PMMA spin coated. Doubly-clamped beam is patterned and sample is developed.

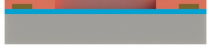

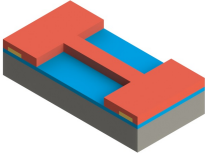

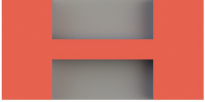
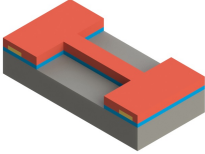


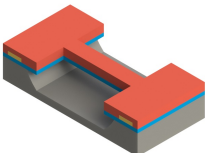

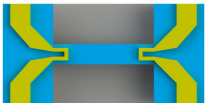
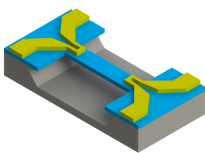
Silicon

Silicon Nitride

PMMA bilayer

Au

Figure 2.20: Fabrication steps of silicon nitride devices - part A

Top View	Side View	Isometric View	Process Step
			60 nm thick copper layer was deposited with e-beam evaporation to be used as an etch mask.
			Inductively Coupled Plasma was used for dry etching: silicon nitride is etched anisotropically with CF_4/CHF_3 gas mixture.
			In order to suspend the nitride device silicon is etched isotropically in ICP with SF_6/CHF_3 gas mixture.
			Cu etch mask is removed with commercially available aluminum wet etchant. Device fully suspended and ready for wirebonding.

Silicon

Silicon Nitride

PMMA bilayer

Cu

Figure 2.21: Fabrication steps of silicon nitride devices - part B

Chapter 3

Transducers for NEMS

As the dimensions of mechanical systems shrunk, the means to *actuate* and *sense* these systems had to adapt as well. These *actuators* and *sensors* are known as *transducers* collectively. “A transducer receives energy from one system and transmits this energy to another system, often in a different form” [38]. In the case of NEMS, the goal is to perturb the nanoscale structure to bend, stretch or twist it and detect the resulting nanomechanical motion which is typically at very high frequencies and with very small amplitudes [39]. The conversion most of the time happens between mechanical, electrical and thermal energy for NEMS.

A nanomechanical resonator can be modeled as a damped harmonic oscillator with the governing equation

$$\ddot{x}(t) + \frac{\omega_o}{Q}\dot{x}(t) + \omega_o^2 x(t) = F_t/m_{eff}, \quad (3.1)$$

where $x(t)$ is the displacement of the resonator, ω_o natural frequency, Q the Quality factor, F_t time dependent excitation and m_{eff} effective mass of the resonator. The actuation transducer converts the electrical drive signal to the F_t term which excites the mechanical motion of the resonator whereas detection transducer converts the mechanical motion, $x(t)$ caused by F_t , to an electrical

signal for read-out.

This work is solely focused on electrothermal (thermoelastic) actuation and piezoresistive detection. There are extensive reviews available in the literature for both MEMS [40, 41] and NEMS [38, 39] transducers.

3.1 Electrothermal Actuation

Electrothermal actuation was one of the first demonstrations of an integrated actuation scheme that can drive a resonator to higher order modes [28]. It relies on heating a bilayer structure to invoke bending. A voltage applied to a small metallic electrode patterned onto the substrate; causes a localized Joule heating [42] which expands both the electrode and the material lying underneath. Since thermal linear expansion coefficient of the metallic electrode and the semiconductor substrate is different, this expansion is nonuniform and causes “thermal stresses that flex the beam towards the substrate” [28]. When this voltage is applied periodically at the resonance frequency of the resonator as an AC voltage, the amplitude of deflection becomes very large.

$$P \sim (V_{AC} \cos(\omega_d t))^2 \sim \frac{V_{AC}^2}{2} + \frac{V_{AC}^2 \cos(2\omega_d t)}{2} \quad (3.2)$$

Due to the nature of Joule heating where the thermal power is proportional to the square of the applied voltage (equation 3.2), the mechanical response of the device occurs at half frequency of the drive voltage. This operation mode is called the 2f mode. If required, a DC biasing could be applied to enforce mechanical response at the same frequency with the drive frequency:

$$P \sim (V_{AC} \cos(\omega_d t) + V_{DC})^2 \sim \frac{V_{AC}^2}{2} + \frac{V_{AC}^2 \cos(2\omega_d t)}{2} + 2V_{AC}V_{DC} \cos(\omega_d t) + V_{DC}^2. \quad (3.3)$$

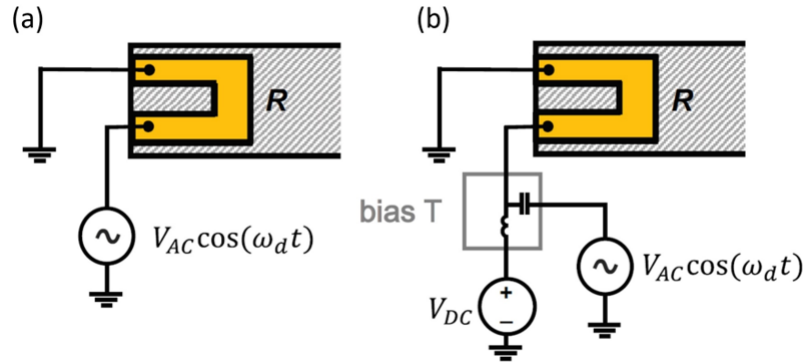


Figure 3.1: AC (a) and DC operation (b) schematics of electrothermal actuation. Reproduced from [39].

Electrothermal actuation's capability of exciting higher order modes of a resonator makes it a suitable candidate for multi-mode applications. Furthermore, it is a purely electronic method and does not require any bulky setups such as optical [43] or magnetomotive [3] methods do. This makes electrothermal actuation convenient for portable sensor applications.

On the other hand electrothermal actuation comes with its own drawbacks. First of all as the actuation is based on heating; the device temperature increases when driven which can become problematic with higher drive voltages. Moreover, since the thermal equilibrium is not instantaneous, the response becomes delayed and efficiency drops rapidly at higher frequencies albeit not until GHz range [28]. Another issue, that can be noticed on eq 3.2 and 3.3, is that the extra drive terms at off-resonance frequencies can interfere with detection. Terms increase with additional drive terms, e.g. when other AC voltages are applied to the drive port such as the extra pump term used in on of the applications that will be discussed in section 4.1.

3.2 Piezoresistive Detection

Piezoresistive detection offers an integrated and purely electronic sensing method to detect nanomechanical motion. Resistance of a material is formulated as

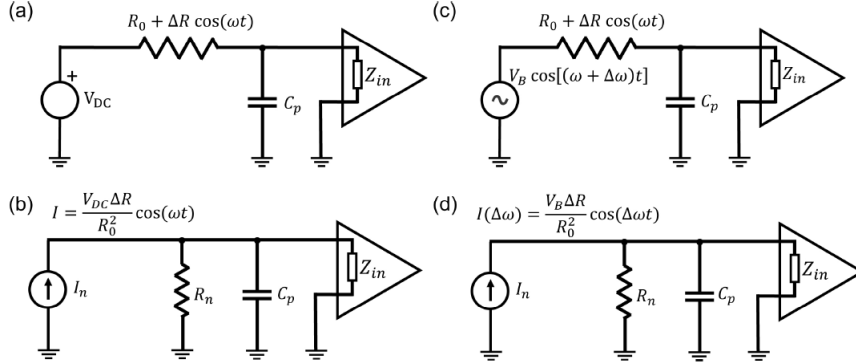


Figure 3.2: DC biasing (a) and AC biasing(c) piezoresistive detection schematics and Norton equivalents respectively (b) and (d). Reproduced from [39].

$R = \rho L/A$ where ρ is the resistivity, L is the length and A is the cross-sectional area of the resistor. There are two types of piezoresistive mechanisms: resistivity (ρ) change and geometric effect. The former is dependent on the change of the electronic band configuration of the material [39], whereas the latter is only dependent on the geometric change of the shape of the electrode. For example, elongation accompanied by reduction in cross-section causes resistance R to increase.

Earlier setbacks of this method was the intrinsically high resistances (5-100 k Ω) of the semiconductor piezoresistive gauges [44]. Combined with parasitic capacitances, circuitry acts as a low pass filter which highly attenuates high frequency signals ($f_{cutoff} = (\pi RC_{par})^{-1}$). In order to overcome this issue, the resistance can be decreased by using metallic electrodes which allows to obtain resistances close to 50 Ω . This is also useful for matching 50 Ω RF lines of the detection instrumentation. Additionally, applying an AC bias instead of DC biasing, will down-mix the signal to a lower frequency which will further prevent attenuation [45].

Detection electrode resistance has both a constant and a variable term: $R_0 + \Delta R \cos(\omega_d t)$ [45]. By applying a bias voltage $V_b(t) = V_b \cos(\omega_b t)$ at frequency $\omega_b = \omega_d + \Delta\omega$ where ω_d is the drive frequency and $\Delta\omega$ is the offset of bias frequency from drive frequency; the output current gains a term $I(\Delta\omega) = (V_b/R_0)(\Delta R/R_0) \cos(\Delta\omega t)$ [39]. Using $\Delta\omega$ sufficiently small ($< 100kHz$), the

down-mixed component is attenuated minimally by parasitic capacitances. The remaining high frequency terms or residual carriers can be removed by a low pass filter.

3.3 Detection Setup

Using electrothermal actuation and piezoresistive down-mixing allows for a fully integrated electronic control of NEMS. It is very convenient compared to bulky and expensive setups used for methods such as optical or magnetomotive detection. In terms of applications, this would allow for portability and mobility and the sensors might be used in the field.

In this work, a custom electronic instrumentation called Dbox was used for measurements. Dbox is essentially a signal down-mixing and acquisition system with its integrated function generators and digital lock-in amplifiers. It can be operated in dual tone to detect two different modes at the same time. A simplified architecture of the equipment can be seen on figure 3.3. Dbox can operate at open loop (frequency domain) for frequency sweeps and closed loop (time domain) for phase locked loop.

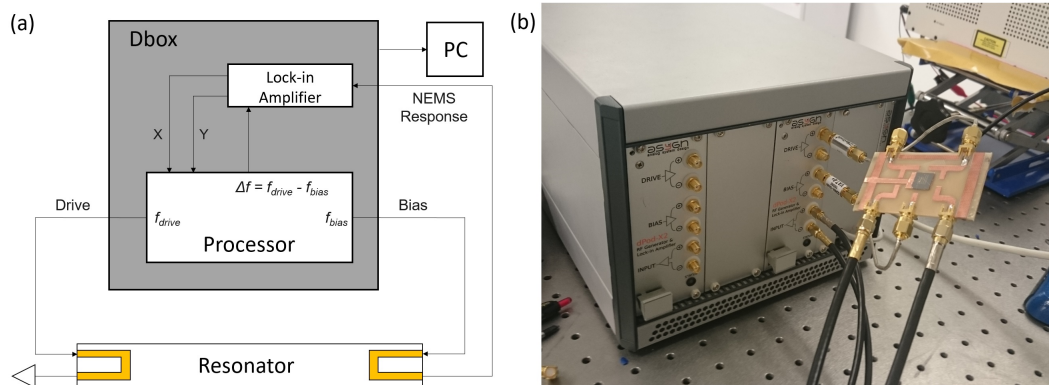


Figure 3.3: Simplified Dbox architecture (a) and its connections to a typical NEMS device. A NEMS device on a PCB connected to a Dbox signal down-mix detection system with SMA coaxial cables which are suitable for RF circuits (b).

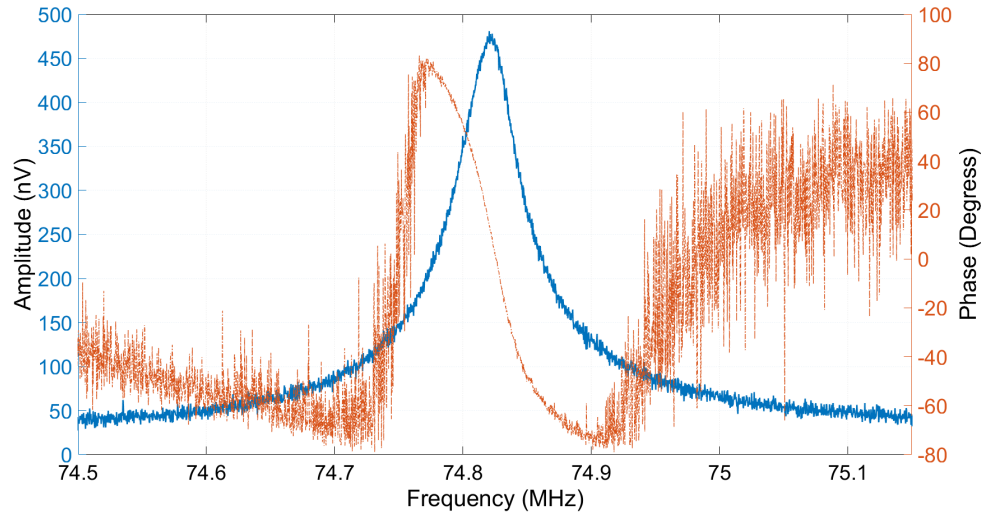


Figure 3.4: Mechanical response of a NEMS around 74.8 MHz detected using Dbox. At the resonance frequency, amplitude is maximum and the phase is zero.

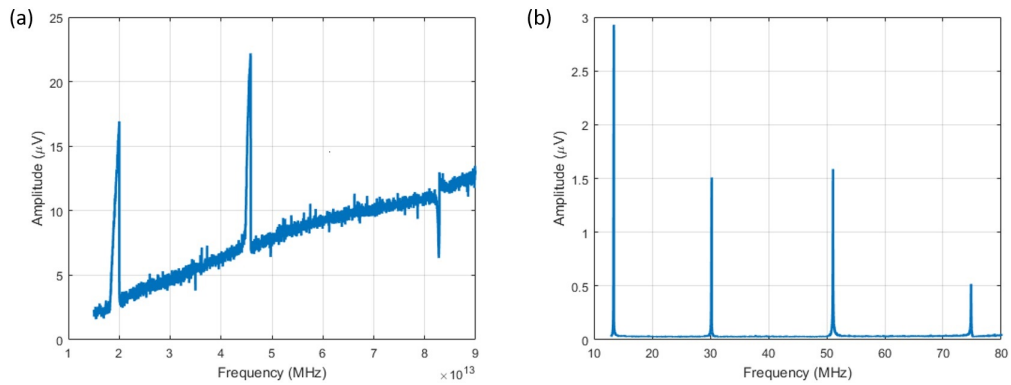


Figure 3.5: Comparison of the response of one of the first iteration of devices, 6μ long, fabricated (a) and final iteration of NEMS, $10 \mu m$ long, with enhanced transduction mechanism (b).

Figure 3.5 shows the mechanical response of one of the earliest NEMS fabricated during this work and as a comparison one of the final iteration NEMS. Enhancing the detection setup by adding a nulling electrode we were able to significantly decrease the background and the noise of the detection signal. Background levels for atmospheric experiments were reduced from earlier few μV (figure 3.5a) to under 50 nV which also did not increase with higher frequencies (figure 3.5b).

Chapter 4

Applications

4.1 Intermodal Coupling Detection for Higher Order Nanomechanical Modes

NEMS provide ultrahigh performance in sensing applications. Sensing performance and functionality can be enhanced by utilizing more than one resonance modes of a NEMS device. However, it is difficult to measure mechanical modes at high frequencies or modes that couple weakly to output transducers. In this application, intermodal coupling is used as a mechanism to enable the detection of modes which are difficult to detect. To implement this method, a probe mode is continuously driven and monitored, while an auxiliary drive signal scans for other modes. As other mechanical modes are excited, they tune the resonance frequency of the probe mode which is detected as a frequency shift. Intermodal coupling can be used as a resource to obtain the spectrum of a mechanical structure even if some of these modes cannot be detected directly.

A common trend in recent years has been the exploitation of higher order modes of a mechanical sensor in mass [14, 15, 46, 47, 48, 49, 50], force [16, 17, 51], stiffness [49, 52] and spatial sensing [18, 53, 54] where the extra information obtained from the higher order modes usually expands the types of measurements

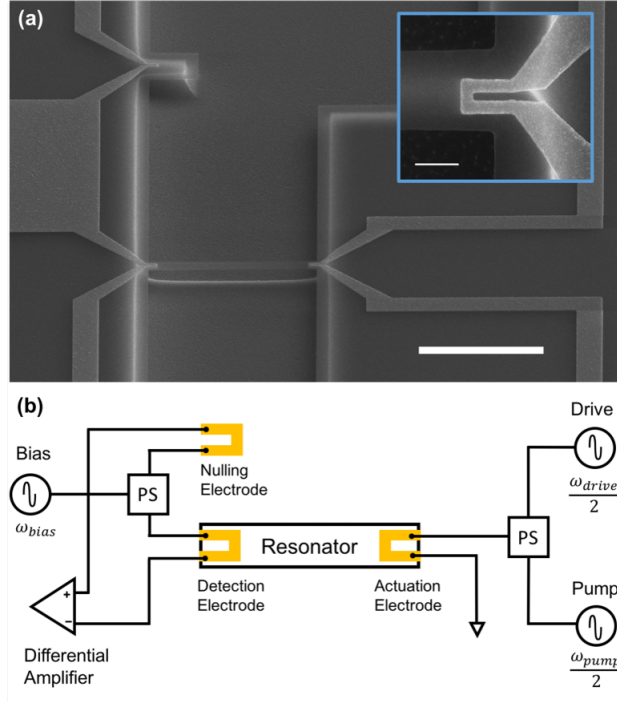


Figure 4.1: Scanning electron micrograph of a nanomechanical resonator along with the electrodes for electrothermal actuation, piezoresistive detection and nulling electrode for background cancellation. Dimensions are $10\mu m \times 850nm \times 100nm$, scale bar is $10\mu m$. Inset shows a close up top view of an electrode, scale bar is $500nm$.

possible and increases sensitivity at the same time [55, 56]. Higher order modes are might be utilized for numerous applications, such as Quality Factor control [12], mechanical vibration registers [57] or phonon cavities [58, 59]. However, access to nanomechanical modes can be challenging under certain conditions. Especially at higher frequencies where the readout schemes are tend to get hindered, e.g. due to increased capacitive coupling of parasitics [10], or when the motion of the mode does not cause a discernible change in the readout transducer, e.g. for even-parity modes in magnetomotive [3] or optomechanical [60] detection.

Flexural modes of a doubly-clamped beam couple to each other anharmonically through the tension generated on the beam [61, 62, 63]. As the beam goes under a flexural motion, the increased tension on the structure tunes the frequency of the other modes. The proposed technique is realized by tracking the

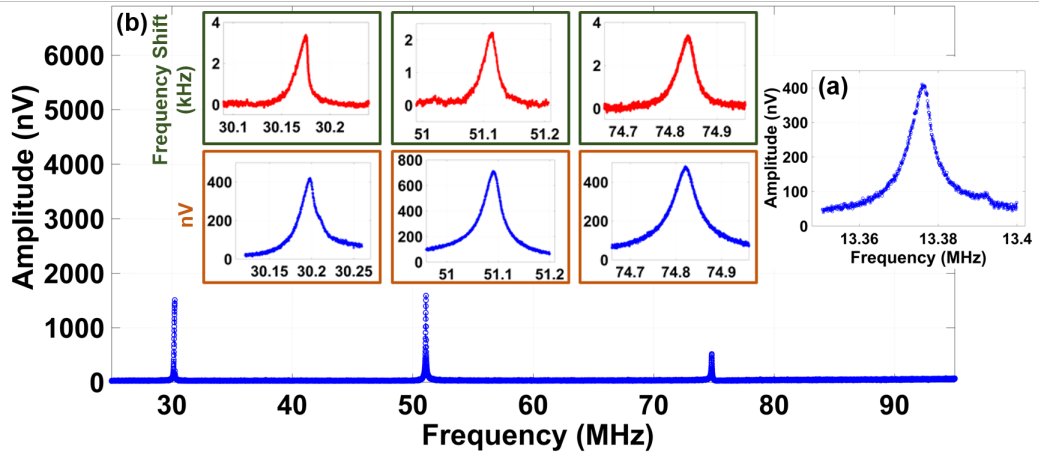


Figure 4.2: (a) Resonant response for the 1st mode at 20 *mTorr*, with drive voltage amplitude of 57 *mV_{pp}* and a quality factor around 3200. (b) Open loop measurement from 25 to 95 MHz, where drive and bias voltage amplitudes are 200 *mV_{pp}* and 673 *mV_{pp}* respectively. Bottom insets show narrower sweeps to observe the linear responses of 2nd, 3rd, 4th out-of-plane modes with drive voltages of 100, 133, and 200 *mV_{pp}* respectively. Top insets demonstrate frequency shift induced on the 1st mode due to intermodal coupling. The applied pump voltage levels for the top row are 118, 151, and 267 *mV_{pp}* for detection of 2nd to 4th mode.

resonance frequency of the fundamental out-of-plane mode of the resonator using a phase-locked loop (PLL), meanwhile sweeping the frequencies of other modes in parallel using the same actuation electrode [61]. This allows for the detection of higher modes which can be driven but cannot be detected with conventional methods. Devices with electrothermal actuation and piezoresistive detection (discussed in chapter 3) was used to investigate intermodal coupling, similar to the ones discussed at section 2.9; yet the proposed technique can be used with any transduction scheme as long as there is a coupling mechanism between modes.

Actuation scheme [28] utilizes the thermal coefficient difference between the gold electrode and silicon nitride beam. An AC drive voltage V_d , at half of the mechanical drive frequency ($\omega_d/2$) is applied to the drive loop, causing Joule heating [42] at the gold electrode. Non-uniform expansion of different materials induces stress on the structure which causes harmonic elastic deformation. The resulting flexural motion of the beam distorts the detection loop at the other end of the beam (Figure 4.1) which alters the resistance of the readout electrode $\Delta R(\omega)$

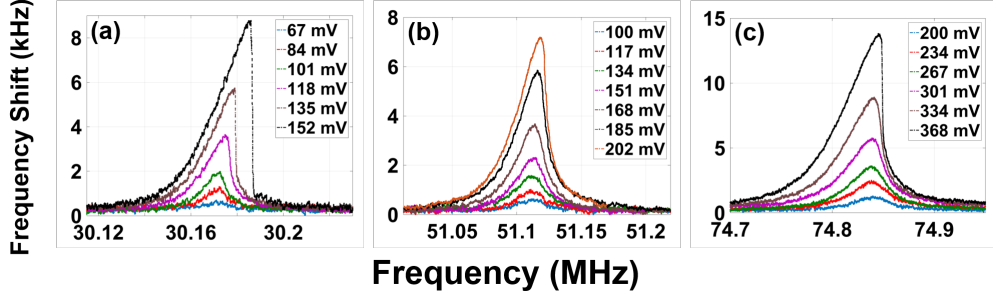


Figure 4.3: Closed loop intermodal coupling measurements between 1st mode and higher order modes. On (a)-(c), increased frequency shift and nonlinear mode coupling between 2nd, 3rd and 4th modes are observed as voltage is increased.

through geometric piezoresistance effect [64]. We use a down-mixing scheme, by applying an AC bias voltage V_b to the detection loop at a frequency of $\omega_d - \Delta\omega$ and detecting the response at the mixed-down frequency of $\Delta\omega$. Detection scheme is further enhanced by incorporating a differential readout circuit, utilizing a nulling electrode, anchored to substrate, to cancel out electronic background (Figure 4.1).

Coupling between flexural modes occurs due to the tension along the beam axis which changes the effective stiffness of the mechanical structure [61]. When the device is actuated, doubly clamped beam undergoes a flexural motion and tries to elongate; since the beam is clamped on both sides it cannot elongate and consequently a longitudinal tension develops on the beam. The resulting tension increases the stiffness, which in turn changes the frequency of the vibrational modes. As a result, when a mode is excited, the frequency of every other mode will get tuned. This can be followed by the equation of motion for the n th mode:

$$m_n \ddot{x}_n + c_n \dot{x}_n + (k_n + \sum g_{nm} x_m^2) x_n = F_n, \quad (4.1)$$

where m_n , c_n , k_n denotes the effective mass, damping coefficient and spring constant respectively. The intermodal coupling constants are shown by g_{nm} . In the experiments, the resonance frequencies of the first two modes are tracked and as other modes are excited, the coupling term in the equation (e.g. $g_{1m} x_m^2 x_1$) increases and causes a discernible frequency shift.

In order to observe mode coupling, the device is first driven at its fundamental mode (Figure 4.2) with an AC drive voltage amplitude of $V_d = 57 mV_{pp}$, which keeps the beam just below the onset of nonlinearity while still allowing for large response. For initial characterization and calibration, open loop sweeps were conducted to detect first four modes of the device in frequency domain (Figure 4.2). Then the resonance frequencies of the first and second modes were tracked by a PLL circuitry sequentially. While the PLL is maintained, higher modes of the device were excited with a simultaneous frequency sweep by superposing a pump signal at frequency ω_p on the actuation electrode. When the open loop sweep is first initiated, a downward frequency shift is observed which is caused by heating of the device by off-resonance AC power. When the pump signal excites a higher mode of the device, an upward frequency shift is observed in the PLL mode, due to increased tension, which indicates the existence of a mechanical mode (bottom row of insets in Figure 4.2). The frequency shifts at the resonance frequencies are in good agreement with the open loop resonance values of these modes.

In this operation mode, additional resonance peaks emerged which do not coincide with those observed in the open loop sweeps (Table 4.2). Most of these peaks are caused by the nature of electrothermal actuation: when two different AC voltages (at frequencies ω_d and ω_p) are applied on the same electrode, they will produce force terms at four different AC frequencies: $2\omega_d$, $2\omega_p$, $(\omega_d + \omega_p)$ and $(|\omega_p - \omega_d|)$. When the hybrid terms, $(\omega_d + \omega_p)$ and $(|\omega_p - \omega_d|)$, coincide with a mechanical resonance, it produces an unintended signal. Such occurrences, however, can be distinguished by checking if any of the hybrid terms overlap with the observed resonances in open loop sweeps.

Using the intermodal coupling/detection method and considering only resonances that overlap in the first and second mode PLLs (Figure 4.2 and Table 4.2). On Figure 4.3 (a-c), the relation between the frequency shift and the pump voltage can be seen for the coupling between the 1st mode and 2nd, 3rd and 4th modes. The location of higher order modes detected with intermodal coupling shows good match with the open loop results.

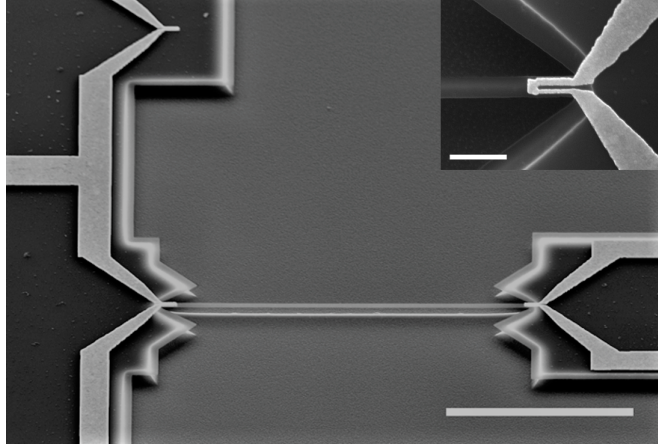


Figure 4.4: A similar NEMS fabricated at Sabanci University as a collaboration. Clamping regions are different from the earlier devices. Dimension are $20\mu m \times 320nm \times 100nm$.

In order to confirm the results another set of experiments were done with similar but different device (Figure 4.4). Both out-of-plane and in-plane modes of this device was measurable. For the next step, resonance frequencies of the first and third (2nd out-of-plane) modes were tracked by a PLL circuitry sequentially at $2 \times 10^{-4} mTorr$ (Figure 4.5). Quality factors of the modes can be also calculated from the frequency shift response of the modes, which agrees with the open loop measurements of the first five modes of the device (Table 4.1). Using the intermodal coupling/detection method, we were able to detect modes up to the 840 MHz (Figure 4.6) while our measurement setup for piezoresistive readout was limited to 0-250 MHz range.

Since the temporal behavior of the PLL is crucial for accurately determining the location of resonances, PLL response time was tested by suddenly de-tuning it away from the resonance and recording its response in reaching back to resonance. Closed loop measurements are further tested with different sweep speeds to ensure that the PLL response is fast enough in tracking resonance line shapes (Figure 4.7). To do this, PLL timescale was kept intact and frequency sweep rate of the higher order modes were varied (i.e. the rate of the disturbance). For fast scans, such as 10ms and 20ms step rates in figure 4.7, PLL cannot react fast enough and there is a distinguishable difference in PLL response as the rate is changed. For

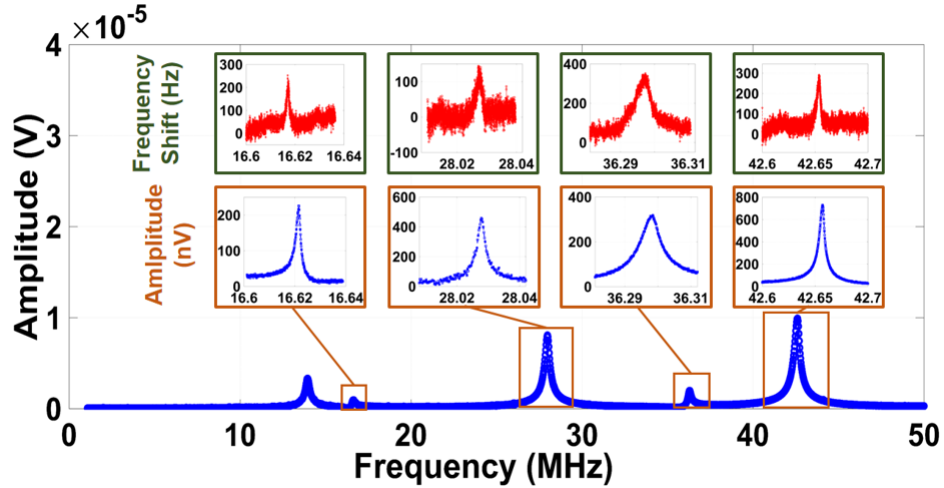


Figure 4.5: Open loop measurement from 1 to 50 MHz in air. Bottom insets demonstrate linear responses of 2nd, 3rd and 4th modes at 2×10^{-4} Torr with drive voltages of 90, 42, 211 and 63 mV_{pp} respectively. Top insets demonstrate frequency shifts induced on the 1st mode due to intermodal coupling. Applied drive voltage for the pump is same as the open loop sweeps.

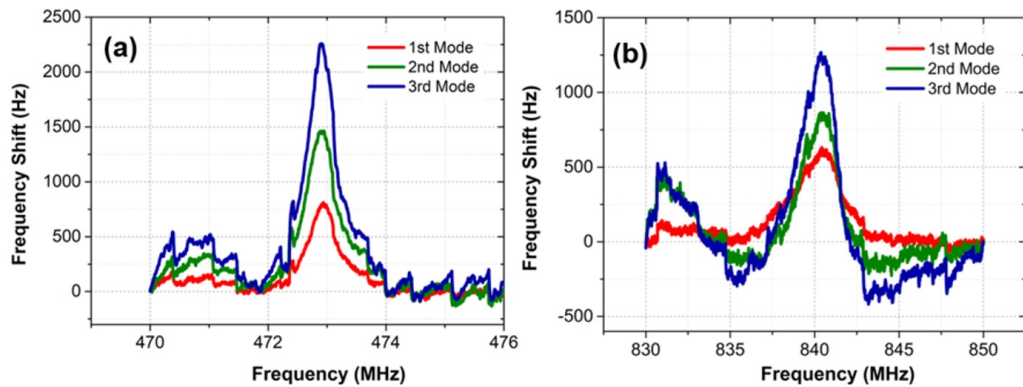


Figure 4.6: Closed-loop intermodal coupling measurements using the first three out-of-plane modes. Two modes were detected around 473 MHz (a) and 840 MHz (b) where all three probe modes experience significant frequency tuning. For both cases drive voltage is 270 mV_{pp} .

Mode Number	Frequency	Open Loop	Closed Loop	Error (%)
	(MHz)	Quality Factor	Quality Factor	
1	13.65	17480	N/A	N/A
2	16.62	11080	11078	0.02
3	28.03	11211	11210	0.009
4	36.3	4270	4537	6.25
5	42.67	9920	10663	7
N/A	473	N/A	844	N/A
N/A	840	N/A	280	N/A

Table 4.1: Quality Factors of the first 5 modes and two ultra-high frequency modes are listed. The comparison of Quality factors as deduced by open-loop and closed-loop (intermodal) measurements are provided. Scale bar is $10 \mu m$, inset $1 \mu m$.

slower scan rates (e.g. 50 ms, 100 ms and 200 ms in figure 4.7), however, PLL response curves become identical, indicating that PLL rate is sufficiently fast to track the resonance curve (i.e. the disturbance).

Intermodal coupling offers a novel method to detect higher vibrational modes of NEMS which can be driven relatively easily but cannot be detected efficiently. As a result, the technique provides a more complete spectrum of nanomechanical modes which can be useful for modeling system parameters accurately or accomplishing multimodal sensing. The method is not limited by the choice of transducers and can be applied to any conventional NEMS detection schemes to improve the read-out strength of high frequency modes.

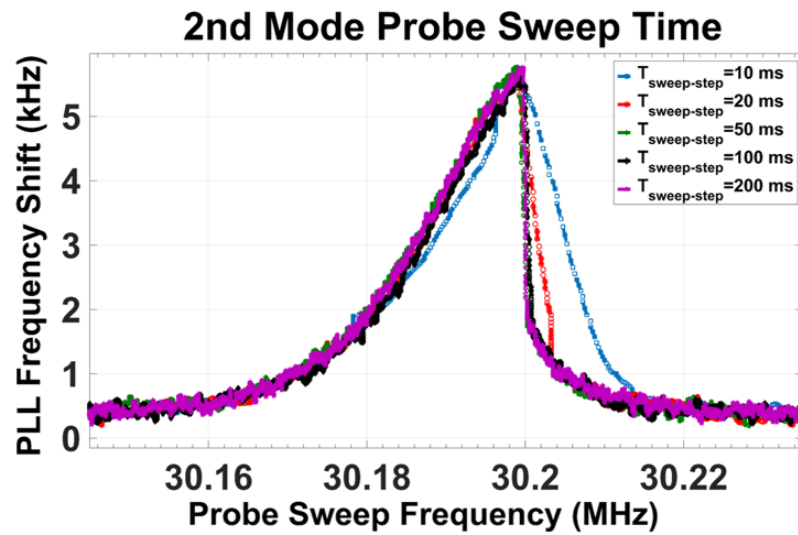


Figure 4.7: PLL mode-coupling measurements between 1st and 2nd mode for rate calibration, taken at different time intervals between unit sweep steps. PLL response behavior converges for sweep time $\geq 50ms$ and rest of the measurements are taken at $100ms$ time between two steps.

<i>PLL Mode</i>	<i>Pump Frequency</i> (ω_p , MHz)	$2\omega_p$ (MHz)	$\omega_D + \omega_p$ (MHz)	$\omega_p - \omega_D$ (MHz)	<i>Remark</i>
1	20.17	40.34	26.89	<u>13.45</u>	$\omega_p - \omega_D$ at 1st mode
1	23.55	47.1	<u>30.27</u>	16.83	$\omega_D + \omega_p$ at 2nd mode
1	25.61	51.22	32.33	18.89	$2\omega_p$ at 3rd mode (also observed directly)
2	25.61	51.22	40.73	10.49	
1	26.81	53.62	33.53	20.09	ω_p at twice 1st mode
2	28.56	57.12	43.68	<u>13.44</u>	$\omega_p - \omega_D$ at 1st mode
2	36.08	72.16	<u>51.2</u>	20.96	$\omega_D + \omega_p$ at 3rd mode
1	36.98	73.97	43.70	<u>30.26</u>	$\omega_p - \omega_D$ at 2nd mode
2	37.45	74.91	52.57	22.33	$2\omega_p$ at 4th mode (also observed directly)
1	37.47	74.94	44.19	30.75	
1	44.49	88.98	<u>51.21</u>	37.77	$\omega_D + \omega_p$ at 3rd mode
2	45.37	90.75	60.49	<u>30.26</u>	$\omega_p - \omega_D$ at 2nd mode
2	50.16	100.33	65.28	35.04	$2\omega_p$ at 6th mode (also observed directly)
1	50.18	100.36	56.9	43.46	
1	57.85	115.70	64.57	<u>51.13</u>	$\omega_p - \omega_D$ at 3rd mode
2	59.68	119.36	<u>74.8</u>	44.56	$\omega_D + \omega_p$ at 4th mode
2	60.29	120.59	75.41	45.17	ω_p at twice 2nd mode
1	64.25	128.50	79.37	49.13	$2\omega_p$ at 7th mode
2	64.29	128.59	71.01	57.57	
2	65.07	130.15	80.19	49.95	$2\omega_p$ at 8th mode
1	65.09	130.18	71.81	58.37	
1	66.31	132.62	81.43	<u>51.19</u>	$\omega_p - \omega_D$ at 3rd mode
1	68.17	136.34	<u>74.89</u>	61.45	$\omega_D + \omega_p$ at 4th mode
2	70.86	141.73	77.58	64.14	$2\omega_p$ at 9th mode
1	70.86	141.73	85.98	55.74	
1	74.81	149.63	81.53	68.09	$2\omega_p$ at 10th mode
2	74.82	149.65	89.94	59.70	

Table 4.2: Features observed during the PLL on first and second mode, ranging from 40 to 150 MHz. The PLL drive frequencies for the first mode is at $\omega_d = 6.72MHz$ and second mode is at $\omega_d = 15.12MHz$.

4.2 Nanomechanical Resonator Platform with Tunable Quality Factor

Nanoelectromechanical Systems can achieve very high Quality (Q) factors which translates to higher sensitivity, low operating power and resonators. Even though a large Q factor is often considered an advantage in most applications, for some niche applications lower Q could be more desirable. One example could be ultra-fast AFMs where a smaller ring-down time is required to have a quicker scan. Since the Q factor is inversely proportional to the dissipation, as can be seen from equation 3.1, the control of dissipation enables us to tune the quality factor and ring-down time [21].

Dissipation for nanomechanical structures can be classified as extrinsic and intrinsic mechanisms [5]. Intrinsic losses are due to imperfections in the crystal structure of the resonator and other phonon-phonon and electron-phonon interactions [5]. Extrinsic sources include: gas damping, coupling losses due to transducers and acoustic radiation/clamping losses.

One option to externally modulate Q factor of a nanomechanical resonator is using *energy sinks*. Energy sinks are linear mechanical oscillators which can increase the dissipation and damping by absorbing the vibrational energy of another structure and store them in their phase space, preventing the energy to leak back to the original tank in a coherent way [65]. Energy sinks were experimentally studied and tested at macro scale [66] and this work is an attempt to implement these energy sinks at nanoscale.

In order to trap the energy from the main tank effectively, an infinite number of sinks would be required. It was shown earlier [65] however, that with the action of a collective but finite number of energy sink resonators, the idealized thermal bath of resonators with infinite degrees of freedom can be mimicked asymptotically. Dynamic response of such a system in macro scale can be modeled as:

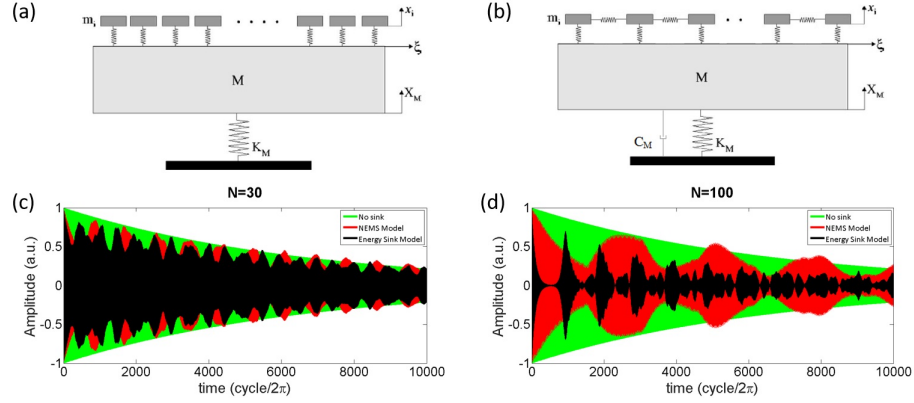


Figure 4.8: Macro scale (a) model versus nano scale (b) model of energy sink interaction. Bottom row shows energy retention simulations based on equation 4.2, comparing 30 energy sinks (c) and 100 energy sinks (d) to macro model. Top row adapted from [65].

$$\begin{aligned}
 M\ddot{x}_M + k_M x_M + \sum_{i=1}^n k_i [x_M - x_i] &= 0, \\
 m_i \ddot{x}_i + k_i [x_i - x_M] &= 0,
 \end{aligned}
 \tag{4.2}$$

where M , x_M , k_M represent mass, displacement and stiffness of the main tank, respectively. m_i , x_i and k_i on the other hand represents the mass, displacement and stiffness of the i^{th} energy sink. In order to successfully mimic infinite oscillators, the finite oscillators must have certain distribution of natural frequencies and optimum distribution can be calculated by [65]:

$$\omega(\xi) = A \left[\frac{(2\xi - 1)}{|2\xi - 1|} \frac{(e^{\alpha|2\xi - 1|} - 1)}{(e^\alpha - 1)} + 1 \right]
 \tag{4.3}$$

where ω is frequency, A the resonance frequency of the main tank and $0 < \xi \leq 1$. The optimal value $\alpha = 2.5$ yields the minimum average energy retention [65].

In an attempt to adapt energy sinks to nano scale, a design where a set of doubly clamped beams in a close proximity to a main tank was envisioned. In this design the main tank would interact with energy sinks via the overhangs that

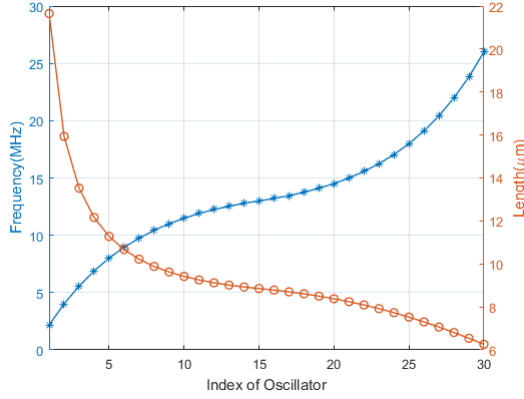


Figure 4.9: Resonance frequency vs. energy sink length calculated, by equation 4.3 to achieve minimum energy retention in main tank.

occur due to under etch caused by isotropic etch of silicon. However, with this configuration the interaction of the sinks and the main tank is slightly different than the macro scale interaction and as a result the physical model is not identical (Figure 4.8 (a) and (b)). In order to determine the effectiveness of the proposed modal energy retention of both the macro scale and nano scale models were simulated (Figure 4.8 c and d) and compared. Results showed that even though macro scale interaction is superior for energy retention, the overhang interaction model is also suitable, especially when higher number of sinks deployed.

In theory, a resonator coupled to energy sinks should have smaller Q factor than an identical resonator with no energy sinks if otherwise identical experimental conditions. Nanoscale energy sinks should increase the dissipation of a nanomechanical resonator, which means decreasing its Q factor. To test this theory three different type of NEMS were fabricated: main tank by itself (Figure 4.12a), main tank accompanied by identical energy sinks (Figure 4.12b) and main tank accompanied by energy sinks with optimum frequency distribution (Figure 4.12c). Initially 30 sinks per device was used. Fabrication of the devices are very similar to steps given on section 2.9 with the addition of energy sinks. According to equation 4.3, required resonant frequencies and corresponding length of sinks to accommodate these frequencies were calculated on shown on figure 4.9. Resonator (main tank) is actuated electrothermally and detected piezoresistively;

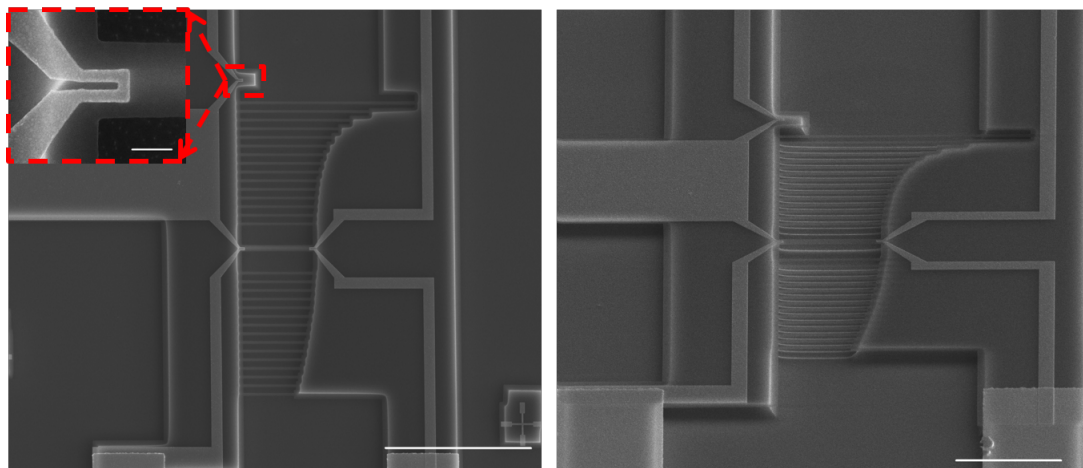


Figure 4.10: Top and tilted view SEM images of a NEMS with frequency distributed energy sinks, scale bars are $20 \mu m$. Inset shows the added nulling electrode to enhance detection by background elimination, scale bar is and $500 nm$ for the inset.

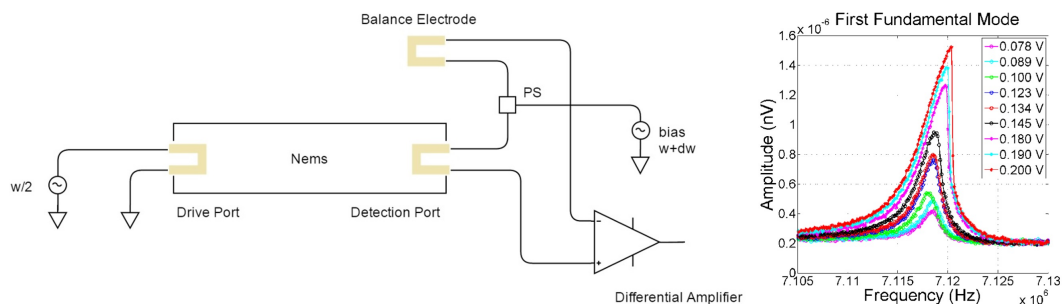


Figure 4.11: Detection scheme of the devices and first fundamental mode driven to nonlinearity.

detection scheme was further enhanced by incorporating a nulling electrode (Figure 4.11) to lower signal background.

The experiments were done at $20 mTorr$. Fundamental mode of each device was measured in an open loop setup with identical drive voltages. Q factors were extracted from the frequency domain response. As expected from the simulations in figure 4.8, the device with no energy sinks had the highest quality factor while the device with optimum frequency distributed energy sinks had the lowest. These preliminary results (figure 4.12) verify the theory and show that energy sinks indeed absorb energy from a main tank at nanoscale. Furthermore, the frequency

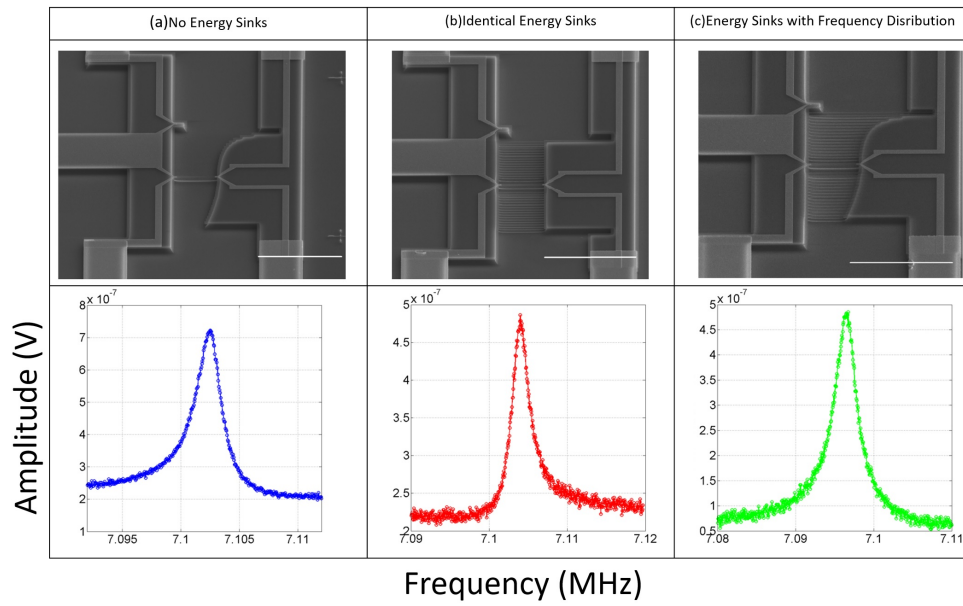


Figure 4.12: Energy sinks experimental results. Resonators with identical dimension but with different energy sinks configuration. Resonator by itself (a), resonator with 30 energy sinks with identical length and frequency (b), resonator with 30 energy sinks with lengths distributed according to eq. 4.3. Bottom row shows 1_{st} mode of each device measured at same conditions. Q factors are (a) 3538, (b) 3262 and (c) 2966. Scale bars are 20 μm .

distribution also seems to affect the energy retention just like it does at macro scale.

There is much to improve on these preliminary results. First of all new measurements in time domain must be done since ring-down time of the main tank would be a much better benchmark for energy retention than Q factor. When more than 70 sinks were deployed the decrease in the Q factor was not at the levels simulated (Bottom row of figure 4.8). This can be attributed to the sink interaction to main tank via the overhangs. Even though the number of sinks was increased the added sinks were more distant to the main tank and thus, the added sinks did not increase coupling effectively. Therefore, this type of overhang coupling is not ideal. A physical interaction between sinks and tank that mimics the macro scale model (4.8) more closely and can maintain larger number sinks without the loss of coupling coefficient might be need. By changing the location of the energy sink resonators and modifying the overhang distance, the coupling strength could be controlled as well. Moreover, for the envisioned real-time Q tuning applications the expected Q drop was more than the achieved 20% decrease with the optimal design. Especially considering earlier work on Q control of AFM tips that achieved 66% [67] and even 90% [68] reduction in Q, albeit the very complex feedback systems that have been utilized, our 20% reduction must be increased.

Chapter 5

Conclusion and Future Work

NEMS bring a lot of opportunities for sensor applications with their unprecedented sensitivity. In this MS study, we utilized top-down microfabrication methods to build multi-mode nanomechanical sensors at Bilkent University. Specifically, electrothermally actuated and piezoresistively detected NEMS that can reach higher order modes deep in to the microwave range targeted for applications that require the information extracted from such modes.

During this work, two new applications utilizing these types of devices were studied. By exploiting the intermodal coupling of a nanomechanical resonator, we proposed a novel method to obtain frequency spectrum of NEMS. We showed experimentally that intermodal coupling can be used to detect higher order modes that cannot be resolved conventionally. We adapted macro scale energy sinks to nanoscale; envisioning a tunable Q factor platform for NEMS. Preliminary results of this work showed that energy sinks do absorb energy of a resonator at nanoscale and the energy retention depends on the frequency distribution of the sinks.

In Chapter 2 fabrication methods applied to build our NEMS were explained. A practical approach was taken to emphasize most important aspects of each method for an operator with some addition of tips and tricks as well. Every step of the fabrication, starting from the commercially available silicon nitride wafers to

wirebonding the completed sensors on a printed circuit board, was done at Bilkent University. Clean rooms and sample preparation techniques were discussed with an emphasis on sample cleaning and handling. We used mostly used E-beam lithography, a direct writing method, for pattern transfer. A PMMA bilayer resist was used to achieve pronounced lift-off profile and we made sure that the ratio of deposited material to resist thickness was 1:3. We did manual alignment of 3 layers to fabricate our NEMS. Thermal evaporated Au, with a very thin layer of Cr underneath, was the material used for contact pads and transducers of the sensors. Cu etch mask was deposited by e-beam evaporation. Since the device dimensions of our design was very small, we deployed an ICP assisted dry etch to achieve shallow etch profile. Two dry etch recipes were developed: CF_4 based recipe was used to anisotropically etch silicon nitride whereas SF_6 based plasma etched the sacrificial silicon layer isotropically. We also used CHF_3 to protect device layer from being etched. The suspended structures were then wirebonded to printed circuit boards for experimentation. During each additive or subtractive step of the fabrication, characterization methods such as SEM and stylus profilometer was utilized to ensure perfect design dimension.

In chapter 3 transducers used in our sensors were presented. We chose to utilize electrothermal drive for our NEMS because it was shown that it is suitable for multi-mode actuation and it is an integrated transducer. To complement electrothermal drive we used piezoresistive detection which is also integrated to the device. Moreover, signal down-mixing was used to enable read out at kHz range. Since all of our transducers were integrated, we did not have to worry about encumbered setups that some of the other actuation methods require. This will also allow for portable sensor applications in the future. We used a custom instrumentation, Dbox, for our electronic measurements of NEMS. Both open loop frequency sweeps and time domain phase locked loop detection was used.

Chapter 4 includes two new applications featuring multi-mode NEMS that we fabricated. Intermodal coupling method is investigated. We showed that each resonant mode of a doubly clamped beam modulates the frequency of the others when excited. When a mode caused flexural motion on the beam an intrinsic stress occurs due to boundary conditions of the beam. Using this as a basis we

tracked the frequency of a mode using a PLL and simultaneously drove other resonant modes and observed frequency shifts. By using intermodal coupling we detected a mechanical mode at 840 MHz while our measurement setup was limited at 250 MHz for conventional detection. Moreover, Q factor information can be extracted from the frequency shift response. On the second application we investigated energy sinks at nano scale. Fabricating devices with and without energy sinks, we measured the Q factor of fundamental mode of each device at identical parameters. Our results show that energy sinks work as intended and the energy absorption depends on the frequency distribution of the sinks.

Our work on energy sinks is far from finished. Interaction model of overhangs must be revised and should mimic the macro scale model better. Time domain measurements should be done to analyze ring down time of a resonator to observe the effects of the energy sinks better. In the end we envision a tunable platform the control the Q factor of a NEMS in real time. However, this goal require at least another few years of work and will be inherited by another graduate student hopefully. There are also other ongoing projects, overseen by my colleagues, in our research group utilizing devices fabricated during this MS study. Çağatay Karakan is working on detection of cancer biomarkers with functionalized NEMS and Ezgi Orhan is researching MALDI assisted mass sensing of biological particles.

Bibliography

- [1] C. Liu, *Foundations of MEMS*. Prentice Hall, 2nd ed., 2012.
- [2] R. P. Feynman, “There’s plenty of room at the bottom,” *Engineering and science*, vol. 23, no. 5, pp. 22–36, 1960.
- [3] A. N. Cleland and M. L. Roukes, “Fabrication of high frequency nanometer scale mechanical resonators from bulk Si crystals,” *Applied Physics Letters*, vol. 69, no. 18, pp. 2653–2655, 1996.
- [4] X. M. Henry Huang, C. A. Zorman, M. Mehregany, and M. L. Roukes, “Nanoelectromechanical systems: Nanodevice motion at microwave frequencies,” *Nature*, vol. 421, pp. 496–496, jan 2003.
- [5] K. L. Ekinici, Y. T. Yang, X. M. H. Huang, and M. L. Roukes, “Balanced electronic detection of displacement in nanoelectromechanical systems,” *Applied Physics Letters*, vol. 81, pp. 2253–2255, sep 2002.
- [6] M. L. Roukes, “Yoctocalorimetry: Phonon counting in nanostructures,” *Physica B: Condensed Matter*, vol. 263-264, no. 264, pp. 1–15, 1999.
- [7] K. L. Ekinici and M. L. Roukes, “Nanoelectromechanical systems,” *Review of Scientific Instruments*, vol. 76, no. 6, p. 1532, 2005.
- [8] K. Schwab, E. A. Henriksen, J. M. Worlock, and M. L. Roukes, “Measurement of the quantum of thermal conductance,” *Nature*, vol. 404, pp. 974–7, apr 2000.
- [9] A. D. O’Connell, M. Hofheinz, M. Ansmann, R. C. Bialczak, M. Lenander, E. Lucero, M. Neeley, D. Sank, H. Wang, M. Weides, J. Wenner, J. M.

- Martinis, and A. N. Cleland, “Quantum ground state and single-phonon control of a mechanical resonator,” *Nature*, vol. 464, pp. 697–703, apr 2010.
- [10] M. Li, E. B. Myers, H. X. Tang, J. S. Aldridge, H. C. McCaig, J. J. Whiting, R. J. Simonson, N. S. Lewis, and M. L. Roukes, “Nanoelectromechanical Resonator Arrays for Ultrafast, Gas-Phase Chromatographic Chemical Analysis,” *Nano Letters*, vol. 10, no. 10, pp. 3899–3903, 2010.
- [11] L. L. Li, E. L. Holthoff, L. A. Shaw, C. B. Burgner, and K. L. Turner, “Noise squeezing controlled parametric bifurcation tracking of MIP-coated microbeam MEMS sensor for TNT explosive gas sensing,” *Microelectromechanical Systems, Journal of*, vol. 23, no. 5, pp. 1228–1236, 2014.
- [12] W. J. Venstra, M. J. Capener, and S. R. Elliott, “Nanomechanical gas sensing with nonlinear resonant cantilevers,” *Nanotechnology*, vol. 25, no. 42, p. 425501, 2014.
- [13] A. K. Naik, M. S. Hanay, W. K. Hiebert, X. L. Feng, and M. L. Roukes, “Towards single-molecule nanomechanical mass spectrometry,” *Nature Nanotechnology*, vol. 4, no. 7, pp. 445–450, 2009.
- [14] M. S. Hanay, S. Kelber, A. K. Naik, D. Chi, S. Hentz, E. C. Bullard, E. Colinet, L. Duraffourg, and M. L. Roukes, “Single-protein nanomechanical mass spectrometry in real time,” *Nature Nanotechnology*, vol. 7, no. 9, pp. 602–608, 2012.
- [15] E. Sage, A. Brenac, T. Alava, R. Morel, C. Dupré, M. S. Hanay, L. Duraffourg, C. Masselon, S. Hentz, and M. L. Roukes, “Neutral particle mass spectrometry with nanomechanical systems,” *Nature communications*, vol. 6, pp. 2–6, 2015.
- [16] E. T. Herruzo, A. P. Perrino, and R. Garcia, “Fast nanomechanical spectroscopy of soft matter,” *Nature communications*, vol. 5, 2014.
- [17] L. M. de Lépinay, B. Pigeau, B. Besga, P. Vincent, P. Poncharal, and O. Arcizet, “A universal and ultrasensitive vectorial nanomechanical sensor for imaging 2D force fields,” *Nature Nanotechnology*, vol. 12, no. 2, pp. 156–162, 2016.

- [18] M. S. Hanay, S. Kelber, C. D. O’Connell, P. Mulvaney, J. E. Sader, and M. L. Roukes, “Inertial imaging with nanomechanical systems,” *Nature Nanotechnology*, vol. 10, no. 4, pp. 339–344, 2015.
- [19] I. Bargatin, E. B. Myers, J. S. Aldridge, C. Marcoux, P. Brianceau, L. Duraffourg, E. Colinet, S. Hentz, P. Andreucci, and M. L. Roukes, “Large-scale integration of nanoelectromechanical systems for gas sensing applications SI,” *Nano Letters*, vol. 12, pp. 1269–1274, mar 2012.
- [20] L. E. Picolet, “Vibration problems in engineering,” *Journal of the Franklin Institute*, vol. 207, no. 2, pp. 286–287, 1929.
- [21] A. N. Cleland and M. L. Roukes, “External control of dissipation in a nanometer-scale radiofrequency mechanical resonator,” *Sensors and Actuators A: Physical*, vol. 72, pp. 256–261, feb 1999.
- [22] S. Franssila, *Introduction to Microfabrication Introduction to Microfabrication Second Edition*. John Wiley & Sons, 2010.
- [23] P. Rai-Choudhury, M. A. McCord, and M. J. Rooks, *Handbook of microlithography, micromachining, and microfabrication. Chapter 2 E. beam lithography*, vol. 1. SPIE Optical Engineering Press, 1997.
- [24] A. Biswas, I. S. Bayer, A. S. Biris, T. Wang, E. Dervishi, and F. Faupel, “Advances in top-down and bottom-up surface nanofabrication: Techniques, applications & future prospects,” *Advances in Colloid and Interface Science*, vol. 170, no. 1-2, pp. 2–27, 2012.
- [25] G. S. May and C. J. Spanos, *Fundamentals of Semiconductor Manufacturing and Process Control*. Wiley, 2006.
- [26] S. A. Campbell, *Engineering at the Micro- and Nanoscale Third Edition*. Oxford University Press, 2008.
- [27] M. J. Madou, *Fundamentals of Microfabrication and Nanotechnology: (Volume II) Manufacturing Techniques for Microfabrication and Nanotechnology*. CRC Press, 3rd ed., 2012.

- [28] I. Bargatin, I. Kozinsky, and M. L. Roukes, “Efficient electrothermal actuation of multiple modes of high-frequency nanoelectromechanical resonators,” *Applied Physics Letters*, vol. 90, no. 9, pp. 1–3, 2007.
- [29] C. A. V. Eysden and J. E. Sader, “Frequency response of cantilever beams immersed in viscous fluids with applications to the atomic force microscope : Arbitrary mode order Frequency response of cantilever beams immersed in viscous fluids with applications to the atomic force microscope :,” *Journal of Applied Physics*, vol. 101, no. 15, pp. 044908–0,044908–11, 1998.
- [30] W. Kern and P. DA, “Cleaning solutions based on hydrogen peroxide for use in silicon semiconductor technology,” *RCA. Review*, vol. 31, no. 2, pp. 187–206, 1970.
- [31] W. Kern and J. E. Soc, “The Evolution of Silicon Wafer Cleaning Technology,” *Journal of the Electrochemical Society*, vol. 137, no. 6, pp. 1887–1892, 1990.
- [32] A. N. Cleland, *Foundations of Nanomechanics - from solid state theory to device applications*. Springer, 2003.
- [33] M. J. Madou, “Fundamentals of Microfabrication and Nanotechnology (Volume III): From MEMS to Bio-MEMS and Bio-NEMS: Manufacturing Techniques and Applications,” CRC Press, 3rd ed., 2012.
- [34] S. a. McAuley, H. Ashraf, L. Atabo, A. Chambers, S. Hall, J. Hopkins, and G. Nicholls, “Silicon micromachining using a high-density plasma source,” *Journal of Physics D: Applied Physics*, vol. 34, no. 18, pp. 2769–2774, 2001.
- [35] Y. J. Lii, J. Jorne, K. C. Cadien, and J. E. J. Schoenholtz, “Plasma etching of silicon in sulfur hexafluoride. Experimental and reactor modeling studies,” vol. 137, pp. 3633–3639, 1990.
- [36] A. Fallis, “Etch Rates for Micromachining Processing,” *Journal of Chemical Information and Modeling*, vol. 53, no. 9, pp. 1689–1699, 2013.

- [37] T. Easwarakhanthan, D. Beyssen, L. Le Brizoual, and J. Bougdira, “Spectroellipsometric analysis of plasma-polymerized fluorocarbon films Spectroellipsometric analysis of CHF 3 plasma-polymerized fluorocarbon films,” *Journal of Vacuum Science & Technology A: Vacuum, Surfaces, and Films*, vol. 24, 2006.
- [38] K. L. Ekinici, “Electromechanical transducers at the nanoscale: Actuation and sensing of motion in nanoelectromechanical systems (NEMS),” *Small*, vol. 1, pp. 786–797, aug 2005.
- [39] T. Kouh, M. S. Hanay, and K. L. Ekinici, “Nanomechanical motion transducers for miniaturized mechanical systems,” *Micromachines*, vol. 8, no. 4, 2017.
- [40] J. W. Judy, “Microelectromechanical systems (MEMS): fabrication, design and applications,” *Smart Materials and Structures*, vol. 10, no. 6, pp. 1115–1134, 2001.
- [41] A. J. Bell, “A classical mechanics model for the interpretation of piezoelectric property data,” *Journal of Applied Physics*, vol. 118, no. 22, 2015.
- [42] L. Jiang, R. Cheung, J. Hedley, M. Hassan, A. J. Harris, J. S. Burdess, M. Mehregany, and C. A. Zorman, “SiC cantilever resonators with electrothermal actuation,” *Sensors and Actuators A: Physical*, vol. 128, no. 2, pp. 376–386, 2006.
- [43] B. Ilic, S. Krylov, K. Aubin, R. Reichenbach, and H. G. Craighead, “Optical excitation of nanoelectromechanical oscillators,” *Applied Physics Letters*, vol. 86, pp. 1–3, may 2005.
- [44] H. Jonathon Mamin, R. P. Ried, B. D. Terris, and D. Rugar, “High-density data storage based on the atomic force microscope,” *Proceedings of the IEEE*, vol. 87, pp. 1014–1027, jun 1999.
- [45] I. Bargatin, E. B. Myers, J. Arlett, B. Gudlewski, and M. L. Roukes, “Sensitive detection of nanomechanical motion using piezoresistive signal down-mixing,” *Applied Physics Letters*, vol. 86, no. 13, p. 133109, 2005.

- [46] S. Dohn, W. Svendsen, A. Boisen, and O. Hansen, “Mass and position determination of attached particles on cantilever based mass sensors,” *Review of Scientific Instruments*, vol. 78, no. 10, p. 103303, 2007.
- [47] S. Dohn, S. Schmid, F. Amiot, and A. Boisen, “Position and mass determination of multiple particles using cantilever based mass sensors,” *Applied Physics Letters*, vol. 97, no. 4, p. 44103, 2010.
- [48] S. Schmid, S. Dohn, and A. Boisen, “Real-time particle mass spectrometry based on resonant micro strings,” *Sensors*, vol. 10, no. 9, pp. 8092–8100, 2010.
- [49] E. Gil-Santos, D. Ramos, J. Martinez, M. Fernandez-Regulez, R. Garcia, A. San Paulo, M. Calleja, J. Tamayo, and J. Martínez, “Nanomechanical mass sensing and stiffness spectrometry based on two-dimensional vibrations of resonant nanowires,” *Nature Nanotechnology*, vol. 5, no. 9, pp. 641–645, 2010.
- [50] S. Olcum, N. Cermak, S. C. Wasserman, and S. R. Manalis, “High-speed multiple-mode mass-sensing resolves dynamic nanoscale mass distributions,” *Nature communications*, vol. 6, 2015.
- [51] R. Garcia and E. T. Herruzo, “The emergence of multifrequency force microscopy,” *Nature nanotechnology*, vol. 7, no. 4, pp. 217–226, 2012.
- [52] J. J. Ruz, J. Tamayo, V. Pini, P. M. Kosaka, and M. Calleja, “Physics of nanomechanical spectrometry of viruses,” *Scientific reports*, vol. 4, p. 6051, 2014.
- [53] T. S. Biswas, J. Xu, N. Miriyala, C. Doolin, T. Thundat, J. P. Davis, and K. S. D. Beach, “Time-Resolved Mass Sensing of a Molecular Adsorbate Nonuniformly Distributed Along a Nanomechanical String,” *Physical Review Applied*, vol. 3, no. 6, p. 64002, 2015.
- [54] S. M. Heinrich and I. Dufour, “Toward Higher-Order Mass Detection: Influence of an Adsorbate’s Rotational Inertia and Eccentricity on the Resonant Response of a Bernoulli-Euler Cantilever Beam,” *Sensors*, vol. 15, no. 11, pp. 29209–29232, 2015.

- [55] M. K. Ghatkesar, V. Barwich, T. Braun, J.-P. Ramseyer, C. Gerber, M. Hegner, H. P. Lang, U. Drechsler, and M. Despont, “Higher modes of vibration increase mass sensitivity in nanomechanical microcantilevers,” *Nanotechnology*, vol. 18, p. 445502, nov 2007.
- [56] D. Ramos, J. Tamayo, J. Mertens, M. Calleja, L. G. Villanueva, and A. Zaballos, “Detection of bacteria based on the thermomechanical noise of a nanomechanical resonator: origin of the response and detection limits,” *Nanotechnology*, vol. 19, p. 035503, jan 2008.
- [57] I. Mahboob, V. Nier, K. Nishiguchi, A. Fujiwara, and H. Yamaguchi, “Multi-mode parametric coupling in an electromechanical resonator,” *Applied Physics Letters*, vol. 103, no. 15, pp. 1–5, 2013.
- [58] I. Mahboob, K. Nishiguchi, H. Okamoto, and H. Yamaguchi, “Phonon-cavity electromechanics,” *Nature Physics*, vol. 8, no. 5, pp. 387–392, 2012.
- [59] R. De Alba, F. Massel, I. R. Storch, T. S. Abhilash, A. Hui, P. L. McEuen, H. G. Craighead, and J. M. Parpia, “Tunable phonon-cavity coupling in graphene membranes,” *Nature Nanotechnology*, vol. 11, no. 9, pp. 741–746, 2016.
- [60] J. N. Westwood-Bachman, Z. Diao, V. T. K. Sauer, D. Bachman, and W. K. Hiebert, “Even nanomechanical modes transduced by integrated photonics,” *Applied Physics Letters*, vol. 108, no. 6, p. 61103, 2016.
- [61] M. H. Matheny, L. G. Villanueva, R. B. Karabalin, J. E. Sader, and M. L. Roukes, “Nonlinear mode-coupling in nanomechanical systems,” *Nano Letters*, vol. 13, no. 4, pp. 1622–1626, 2013.
- [62] H. J. R. Westra, M. Poot, H. S. J. Van Der Zant, and W. J. Venstra, “Nonlinear modal interactions in clamped-clamped mechanical resonators,” *Physical review letters*, vol. 105, no. 11, p. 117205, 2010.
- [63] A. Eichler, M. del Álamo Ruiz, J. A. Plaza, and A. Bachtold, “Strong coupling between mechanical modes in a nanotube resonator,” *Physical review letters*, vol. 109, no. 2, p. 25503, 2012.

- [64] M. Li, H. X. Tang, and M. L. Roukes, “Ultra-sensitive NEMS-based cantilevers for sensing, scanned probe and very high-frequency applications,” *Nature nanotechnology*, vol. 2, no. 2, pp. 114–120, 2007.
- [65] I. M. Koc, A. Carcaterra, Z. Xu, and A. Akay, “Energy Sinks: Vibration Absorption by an Optimal Set of Undamped Oscillators,” *The Journal of the Acoustical Society of America*, vol. 118, no. 5, p. 3031, 2005.
- [66] A. Akay, Z. Xu, A. Carcaterra, and I. M. Koc, “Experiments on Vibration Absorption using Energy Sinks,” *The Journal of the Acoustical Society of America*, vol. 118, no. 5, p. 3043, 2005.
- [67] J. Jahng, M. Lee, H. Noh, Y. Seo, and W. Jhe, “Active Q control in tuning-fork-based atomic force microscopy,” *Applied Physics Letters*, vol. 91, no. 2, pp. 2007–2009, 2007.
- [68] T. Sulchek, R. Hsieh, J. D. Adams, G. G. Yaralioglu, S. C. Minne, C. F. Quate, J. P. Cleveland, A. Atalar, and D. M. Adderton, “High-speed tapping mode imaging with active Q control for atomic force microscopy,” *Applied Physics Letters*, vol. 76, pp. 1473–1475, mar 2000.

Appendix A

RCA Clean

RCA-1:

- 1 part of aqueous NH_4OH (ammonium hydroxide, 29% by weight of NH_3) added to 5 parts of DI water.
- Solution heated up to 75°C . Solution removed from hot plate.
- 1 part of aqueous H_2O_2 (hydrogen peroxide, 30%) added to solution.
- 2 minutes after bubbles formed soak sample in the solution for 15 minutes.
- Rinse with DI water.

RCA-2:

- 1 part of aqueous HCl (hydrochloric acid, 37% by weight) added to 6 parts of DI Solution heated up to 75°C
- Solution heated up to 75°C . Solution removed from hot plate.
- 1 part of aqueous H_2O_2 (hydrogen peroxide, 30%) added to solution.
- 2 minutes after bubbles formed soak sample in the solution for 15 minutes.

- Rinse with DI water.

HF dip:

- 10 second dip in room temperature BOE(1:7)
- Rinse with DI water.

Appendix B

E-beam Lithography Operation Checklist

Atakan B. ARI Feb. 23th 2017 v4

SAMPLE PLACEMENT AND PREPARATION

- Place the sample and make sure you memorize the orientation of it.
- Blow N2 gently to sweep any dust or contaminants.
- If the sample is very smooth and bare, which makes it hard to focus, you can make a little scratch with your tweezer, preferably a metal sharp one, near the clamp.
- Push the chamber door for 20 seconds after pressing pump from the SEM control screen.

ADJUSTMENT for bare samples(No Alignment Procedure)

- Go to Ata-Start which is located on the bottom left of the stage.
- Locate bottom left corner of your sample.

- Align the bottom of your chip make it parallel to screen.
- Make rough focus (x10k) then get the working distance to 5 mm. Watch the movement of the stage and make sure it doesn't touches the Ebeam Gun!
- Go to bottom left corner of your sample and adjust it as the 'Origin'(0,0 on ELPHY Plus(EP).
- Adjust the same point as the 1st point for angle correction.
- Move to the bottom right corner of your sample and adjust it as the 2nd point for angle correction.
- Adjust Angle correction.
- Now bottom left corner of your sample is your origin and x coordinate increases to right and y coordinate increases upwards relative to the screen.

SETTING THE BEAM CURRENT and STEP SIZE

- Set your Beam Voltage and Beam Current to desired values.
- Get a rough focus on piece of dirt (x20k)
- Save this location on stage coordinates. (Don't alter other positions please, use your own.)
- Tick off Z, T and R coordinates and move to Faraday Cage position on the list.
- Center the Faraday Cage and zoom to maximum magnification.
- Write down the Current from the MicroAmmeter.
- Set your desired Writefield. Make sure your working area is equal to or smaller than your writefield!
- Open the calculator on patterning tab.

- Write the current form Ammeter and Step size.
- Calculate the dwell time.
- Make sure Beam speed is not higher than 11 mm/s. If so increase the step size. If the step size is not small enough for your minimum feature size you need to lower your beam current.

SETTING POSITION LIST AND PATTERNING

- Go back to saved location.
- Focus at least at x75k, higher the better.
- Get rid of any stigmatism.
- Set your desired Writefield from EP.
- Drag your design to a positionlist.
- Enter desired dose and U,V coordinates.
- Make sure your Writefield is larger than your Working Area!!!
- Make sure the pattern you want to write is confined within the Working Area.
- Check the 'times' from parameters. If the result is absurd it means something is wrong.
- Before starting scanning drive to position and check the U,V and X,Y coordinates and see it matches the values you set.
- If everything is set you can start scanning. If there are more than one item on the list you can choose 'scan all' from scan tab.